



**HAL**  
open science

## **Cirques have growth spurts during deglacial and interglacial periods: Evidence from $^{10}\text{Be}$ and $^{26}\text{Al}$ nuclide inventories in the central and eastern Pyrenees**

Y. Crest, M Delmas, Regis Braucher, Y. Gunnell, M Calvet, A.S.T.E.R. Team

### ► To cite this version:

Y. Crest, M Delmas, Regis Braucher, Y. Gunnell, M Calvet, et al.. Cirques have growth spurts during deglacial and interglacial periods: Evidence from  $^{10}\text{Be}$  and  $^{26}\text{Al}$  nuclide inventories in the central and eastern Pyrenees. *Geomorphology*, 2017, 278, pp.60 - 77. 10.1016/j.geomorph.2016.10.035 . hal-01420871

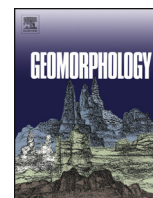
**HAL Id: hal-01420871**

**<https://amu.hal.science/hal-01420871>**

Submitted on 21 Dec 2016

**HAL** is a multi-disciplinary open access archive for the deposit and dissemination of scientific research documents, whether they are published or not. The documents may come from teaching and research institutions in France or abroad, or from public or private research centers.

L'archive ouverte pluridisciplinaire **HAL**, est destinée au dépôt et à la diffusion de documents scientifiques de niveau recherche, publiés ou non, émanant des établissements d'enseignement et de recherche français ou étrangers, des laboratoires publics ou privés.



# Cirques have growth spurts during deglacial and interglacial periods: Evidence from $^{10}\text{Be}$ and $^{26}\text{Al}$ nuclide inventories in the central and eastern Pyrenees



Y. Crest <sup>a,\*</sup>, M. Delmas <sup>a</sup>, R. Braucher <sup>b</sup>, Y. Gunnell <sup>c</sup>, M. Calvet <sup>a</sup>, ASTER Team <sup>b,1</sup>:

<sup>a</sup> Univ Perpignan Via-Domitia, UMR 7194 CNRS Histoire Naturelle de l'Homme Préhistorique, 66860 Perpignan Cedex, France

<sup>b</sup> Aix-Marseille Université, CNRS-IRD-Collège de France, UMR 34 CEREGE, Technopôle de l'Environnement Arbois-Méditerranée, BP80, 13545 Aix-en-Provence, France

<sup>c</sup> Univ Lyon Lumière, Department of Geography, UMR 5600 CNRS Environnement Ville Société, 5 avenue Pierre Mendès-France, F-69676 Bron, France

## ARTICLE INFO

### Article history:

Received 14 June 2016

Received in revised form 25 October 2016

Accepted 27 October 2016

Available online 29 October 2016

### Keywords:

Cirque

Denudation rate

Cosmogenic nuclide dating

Buzzsaw

Pyrenees

## ABSTRACT

Cirques are emblematic landforms of alpine landscapes. The statistical distribution of cirque-floor elevations is used to infer glacial equilibrium-line altitude, and the age of their frontal moraines for reconstructing glacial chronologies. Very few studies, however, have sought to measure cirque-floor and supraglacial ridgetop bedrock downwearing rates in order to confront these denudation estimates with theoretical models of Quaternary mountain landscape evolution. Here we use  $^{10}\text{Be}$  nuclide samples ( $n = 36$ ) from moraines, bedrock steps, and supraglacial ridgetops among a population of cirques in the east-central Pyrenees in order to quantify denudation in the landscape and detect whether the mountain topography bears any relevance to the glacial buzzsaw hypothesis. Minimum exposure ages (MEAs) obtained for a succession of moraines spanning the Oldest Dryas to the Holocene produced a deglaciation chronology for three different Pyrenean ranges: Maladeta, Bassiès, and Carlit. Based on a series of corrections, calibrations, and chronostratigraphic tuning procedures, MEAs on ice-polished bedrock exposures were further used to model denudation depths at nested timescales during the Würm, the Younger Dryas, and the Holocene. Results show that subglacial cirque-floor denudation was lower during glacial periods (Würm:  $\sim 10$  mm/ka) than during deglacial and interglacial periods (tens to hundreds of mm/ka). The relative inefficiency of glacial denudation in the cirque zone during the Würm would have resulted from (i) cold-based and/or (ii) low-gradient glaciers situated in the upper reaches of the icefield; and/or from (iii) glacier-load starvation because of arrested clast supply from supraglacial rockslopes situated in the permafrost zone. Denudation peaked during the Younger Dryas and Holocene glacial advances, a time when cirque glaciers became steeper, warmer-based, and when frost cracking weakened supraglacial ridgetops, thus enhancing subglacial erosion by providing debris to the sliding glacier base. Cirques, therefore, grow faster during more temperate periods of cirque glaciation than under full glacial conditions. Another key finding was the very low rates of ridgetop lowering averaged over the Würm and Holocene (10–25 mm/ka). A comparison of the denudation rates obtained from the cirque zone with regional estimates of crustal uplift indicates that the alpine topography is not in a steady state. The low intensity of glacial denudation failed to bring the topography to a buzzsaw equilibrium state.

© 2016 Elsevier B.V. All rights reserved.

## 1. Introduction

The idea that feedback between climate and crustal uplift drove accelerated mountain uplift during the late Cenozoic has been an underlying hypothesis of research in Earth sciences (Molnar and England, 1990; Small and Anderson, 1995; Whipple et al., 1999; Whipple, 2009; Champagnac et al., 2012). Among the various geomorphic agents contributing to denudation, glaciers are recognized as being very efficient

at reshaping mountain topography and generating isostatic-driven uplift. This statement is based on a growing body of quantitative data acquired worldwide, using a range of methods of measurement and spanning different spatial and timescales (Champagnac et al., 2014). Low-temperature thermochronology (LTT: e.g., apatite fission-track analysis, apatite helium, and  $^4\text{He}/^3\text{He}$  dating) captures long-term denudation rates ( $10^5$  to  $10^8$  years; Shuster et al., 2005, 2011; Ehlers et al., 2006; Densmore et al., 2007; Berger et al., 2008; Thomson et al., 2010; Valla et al., 2011). In a variety of mountain ranges, results based on these methods have recorded high denudation rates since 6 Ma and accelerated denudation after 2 Ma (review in Herman et al., 2013). This acceleration has been attributed to several climate-changing events during the late Cenozoic, e.g., global cooling and onset of glaciation in

\* Corresponding author at: Université de Perpignan – Via Domitia, UMR 7194 CNRS, 52 avenue Paul Alduy, 66860 Perpignan, France.

E-mail address: [yannick.crest@univ-perp.fr](mailto:yannick.crest@univ-perp.fr) (Y. Crest).

<sup>1</sup> ASTER Team: G. Aumaitre, D.L. Bourlès, K. Keddadouche.

the northern hemisphere, activation of the Gulf Stream after closing of the isthmus of Panama ca. 4 Ma. These changes are recorded at all latitudes but appear sharpest among mid-latitude mountain belts, which during the Pleistocene hosted temperate-based and polythermal glaciers (Herman et al., 2013; Champagnac et al., 2014). Lower denudation values recorded among a variety of high-latitude mountain ranges are ascribed, accordingly, to the presence of cold-based glaciers (e.g., south Patagonia: Thomson et al., 2010; Koppes et al., 2015; northwest Svalbard: Gjermundsen et al., 2015). Sediment fluxes from current proglacial rivers and Holocene outwash sequences in fjords or lakes record denudation indirectly over shorter timescales (10 to 10<sup>4</sup> years) than LTT and provide catchment-averaged glacial denudation rates (Delmas et al., 2009). Case studies based on these methods have tended to provide high denudation rates (Hallet et al., 1996; Koppes and Hallet, 2006; Fernandez et al., 2011), but reviews report a wide spectrum of values spanning four orders of magnitude (from 0.001 to 10 mm/a; Delmas et al., 2009) and show that glacial and fluvial denudation rates can be similar (1 to 10 mm/a) under specific circumstances such as rapid tectonic uplift (Koppes and Montgomery, 2009).

In the same way, many numerical models based on basal ice sliding velocity and discharge show that Pleistocene glaciations have greatly controlled landscape evolution. The impacts of glacial denudation on topography have been argued to increase local relief and topographic steepness, either by overdeepening glacial trunk valleys (MacGregor et al., 2000; Valla et al., 2011) or by increasing preglacial topographic roughness (Sternai et al., 2015). The overall result is one of enhanced energy in the geomorphic system. Glacial erosion in tectonically active mountain ranges is also known to generate a characteristic hypsometric signature (deemed typical of the so-called glacial buzzsaw) displaying (i) a large proportion of land area occurring at the level of some Quaternary equilibrium-line altitude (e.g., the Quaternary average ELA, or QA-ELA, of Mitchell and Humphries, 2014); (ii) a limited elevation band immediately above this QA-ELA; and (iii) a tendency to produce a network of narrow ridges and peaks (Brozović et al., 1997; Brocklehurst and Whipple, 2002, 2004; Mitchell and Montgomery, 2006; Foster et al., 2008).

Given that the QA-ELA concept is expedient but problematic in a number of ways (see Evans et al., 2015; Mitchell and Humphries, 2015; Robl et al., 2015a), for the purpose of this study we settle instead for the regionally established notion of an average Pleistocene ELA, which was defined for the central and eastern Pyrenees using standard methods of ELA delimitation reported in Delmas et al. (2015). Within the buzzsaw narrative, altitude limits on ridgetops have been attributed to cirque floors acting as local base levels that control slope processes on cirque headwalls and generate sharpened arêtes by receding the headwall intersection (Schmidt and Montgomery, 1995; Egholm et al., 2009; Anders et al., 2010). Coalescing cirques are expected to promote the development of uniform lowering of ridgetops. This is advocated as one possible way of explaining crest and summit accordance in alpine settings (the 'Gipffelur' problem of Penck, 1919), which nonetheless is also observed in unglaciated mountain ranges where regular patterns of fluvial dissection can appear to constrain ridgetops to a narrow elevation band.

The alpine cirque zone is the main focus of this study, with implications for the buzzsaw hypothesis and in a context where denudation rates responsible for alpine cirque development have remained poorly documented (see Barr and Spagnolo, 2015, Table 1 therein). Moreover, most publications on the quantification of cirque growth provide mean denudation values, without any distinction between the downwearing and backwearing components, because data are based either on cirque landform change (Andrews and LeMasurier, 1973; Olyphant, 1981; Brook et al., 2006) or on sediment volume output by cirque glaciers (Reheis, 1975; Anderson, 1978; Mills, 1979; Larsen and Mangerud, 1981; Hicks et al., 1990; Bogen, 1996). In the latter case, clast roundedness analysis has been used to discriminate between debris generated by subglacial processes and those generated by supraglacial hillslope processes operating on cirque headwalls (including rockfall, frost cracking, snow avalanches, etc.). Data thus obtained report headward

denudation rates that are consistently lower than downwearing values, with 5 to 40% of the total sediment volume originating from headwalls against 95 to 60% from the subglacial bedrock (Reheis, 1975; Anderson, 1978; Larsen and Mangerud, 1981; Hicks et al., 1990). In contrast, a sediment budget involving a detailed inventory of sediment sources, transport pathways (supra-, sub- and englacial iceload, river suspended load and bedload, etc.), and storage sites in a glaciated alpine cirque of British Columbia (Canada) yielded greater headwall denudation rates (0.2–5.2 mm/a) than vertical subglacial cirque deepening rates (0.9–1.2 mm/a; Sanders et al., 2013). Those results were based on a quantification of debris accumulations produced and stored in the sediment system and relied on a large array of field measurements and remote sensing data. Overall, published data on cirque denudation rates compiled in Barr and Spagnolo (2015) span either very short (a few years to a few 10<sup>3</sup> years) or very long timescales (at least the entire Pleistocene in the case of estimates of landform change among cirques). With the exception of Sanders et al. (2013), none provide data on cirque growth patterns during the interval of an entire Pleistocene glacial/interglacial cycle, and none are based on in situ measurements likely to offer a distinction between back- and downwearing. Theoretical models have hypothesized, for example, that cirques grow mainly during interglacial periods, i.e., at times when glaciers are restricted to the cirque zone rather than during periods of extensive (i.e., icefield or icesheet) glaciation (Cook and Swift, 2012; Barr and Spagnolo, 2015).

Here we explore and test these ideas based on field measurements. We investigate the variability of glacial denudation rates at nested timescales within the alpine cirque zone of a mid-latitude intracontinental orogen, the Pyrenees, based on 36 measurements of cosmogenic <sup>10</sup>Be produced in situ obtained from three different Pyrenean ranges and measured among three kinds of rock surface: (i) boulders embedded in successive generations of frontal or lateral moraines, which are used as tools for establishing the chronology of cirque glaciation; (ii) polished bedrock steps, which are used to quantify glacial downwearing rates on cirque floors at nested timescales (entire Würmian glaciation cycle, Younger Dryas and Holocene readvances); and (iii) bedrock exposures on adjacent supraglacial ridgetops, which allow comparisons with glacial denudation on the cirque floors. The study focuses on three crystalline massifs located in the most elevated part of the mountain belt (Fig. 1), each having undergone somewhat contrasting impacts from the Pleistocene icefields. The Maladeta range (Pico de Aneto: 3404 m) is the most elevated massif of the Pyrenees and still bears a few small residual glaciers and a number of Holocene moraines. The Bassiès and Carlit ranges, which occur ~60 and ~100 km to the east of the Maladeta, respectively, are currently entirely deglaciated and bear no obvious vestiges of Holocene glacial landforms. The contrast in glacial histories and hypsometric attributes (Figs. 2, 3, and 4) between the three massifs provides additional value to the purpose of comparing these ranges. The aim is (i) to quantify in each case the rates of cirque-floor and ridgetop downwearing over the time scales of the Würm (regional icefield with large outlet glaciers), the Younger Dryas, and the Neoglacial (regrowth of cirque glaciers in the mid-Holocene after partial or complete deglaciation during the early Holocene; Matthews, 2013), respectively; (ii) to discuss inferences about the effects of glaciation on alpine topography in the Pyrenees; and (iii) to compare the results with other mid-latitude mountain ranges.

## 2. Geological and geomorphological settings

### 2.1. Long-term landscape evolution

The Pyrenees formed as a result of collision between Europe and the Iberian microplate during and after the late Cretaceous. The Axial Zone forms the inner and most elevated core of the mountain belt and consists of a Paleozoic basement—mainly granite, orthogneiss, and metasedimentary rocks. To its north and south, the Axial Zone is flanked by a succession of fold and thrust belts dominated by Mesozoic and

**Table 1**  
<sup>10</sup>Be cosmogenic nuclide results and derived apparent exposure ages for cirque floors and moraines.

Sample ID	Location (glacial stage)	Field source	<sup>10</sup> Be concentration ( $\times 10^4$ at/g $\pm 1\sigma$ )	MEA (ka $\pm 1\sigma$ )
Maladeta–Aneto				
AN01	Aigualluts	Boulder	26.86 $\pm$ 1.80	16.16 $\pm$ 1.08
AN02		Boulder	25.16 $\pm$ 2.30	14.83 $\pm$ 1.36
MA03		Polished surface	33.20 $\pm$ 1.18	14.31 $\pm$ 0.51
MA04	Renclusa	Boulder	33.59 $\pm$ 1.05	12.12 $\pm$ 0.38
MA05		Boulder	19.43 $\pm$ 1.02	8.51 $\pm$ 0.45
MA06		Boulder	30.90 $\pm$ 1.33	13.59 $\pm$ 0.58
MA07		Polished surface	33.14 $\pm$ 1.05	13.50 $\pm$ 0.43
MA08		Polished surface	66.42 $\pm$ 2.05	23.94 $\pm$ 0.74
AN09		Polished surface	33.08 $\pm$ 1.05	14.00 $\pm$ 0.45
AN10		Polished surface	30.31 $\pm$ 0.95	12.98 $\pm$ 0.41
MA11	LIA	Polished surface	12.78 $\pm$ 0.43	4.79 $\pm$ 0.16
MA12		Polished surface	16.43 $\pm$ 0.63	6.06 $\pm$ 0.23
AN13		Polished surface	19.43 $\pm$ 0.68	7.10 $\pm$ 0.25
AN14		Polished surface	21.51 $\pm$ 0.71	7.88 $\pm$ 0.26
Bassiès				
BA15	Legunabens	Boulder	23.37 $\pm$ 1.43	15.40 $\pm$ 0.94
BA16		Polished surface	24.31 $\pm$ 1.19	15.83 $\pm$ 0.77
BA17	Mouscadous	Boulder	20.44 $\pm$ 1.86	11.85 $\pm$ 1.08
BA18		Boulder	19.47 $\pm$ 1.43	11.36 $\pm$ 0.83
BA19		Polished surface	13.36 $\pm$ 0.80	8.66 $\pm$ 0.52
BA20		Polished surface	18.93 $\pm$ 1.04	12.26 $\pm$ 0.67
BA21		Polished surface	35.75 $\pm$ 1.21	15.01 $\pm$ 0.51
BA22		Polished surface	33.06 $\pm$ 1.04	14.96 $\pm$ 0.47
BA23		Polished surface	28.74 $\pm$ 0.98	13.41 $\pm$ 0.46
BA24		Polished surface	18.95 $\pm$ 0.59	8.68 $\pm$ 0.27
Carlit <sup>a</sup>				
CAC25	Cometa d'Espagne	Polished surface	23.64 $\pm$ 3.85	10.98 $\pm$ 1.79
CAC26		Polished surface	22.33 $\pm$ 2.75	12.11 $\pm$ 1.49
CAC27		Polished surface	28.08 $\pm$ 6.33	12.06 $\pm$ 2.72
CAC28		Polished surface	63.73 $\pm$ 3.34	27.94 $\pm$ 1.47
CAL29	Llat	Polished surface	58.37 $\pm$ 9.63	26.81 $\pm$ 4.42
CAL30		Polished surface	57.67 $\pm$ 8.68	26.31 $\pm$ 3.96
CAL31		Polished surface	20.86 $\pm$ 2.68	21.71 $\pm$ 2.97

<sup>a</sup> The CAL and CAC samples present wider uncertainty intervals because measurements were carried out in 2005 and 2006 at the Tandétron in Gif-sur-Yvette, France, an AMS with substantially lower precision than ASTER.

Paleogene sedimentary rocks. Collision-related deformation in the central and eastern Pyrenees ceased ca. 20–25 Ma, when the main focus of crustal deformation resulting from the convergence between Europe and Africa transferred from the Pyrenees to the Betic Cordillera (Vergés et al., 2002). The collisional stages are well documented by

LTT, which records 6 to 9 km of crustal denudation during the Paleogene, followed by evidence of a sharp decline since ~25–30 Ma (Gibson et al., 2007; Gunnell et al., 2008, 2009; Metcalf et al., 2009; Fillon and van der Beek, 2012). By 30–28 Ma the eastern Pyrenees, probably as far west as the Maladeta massif (Ortuño et al., 2008, 2013), were

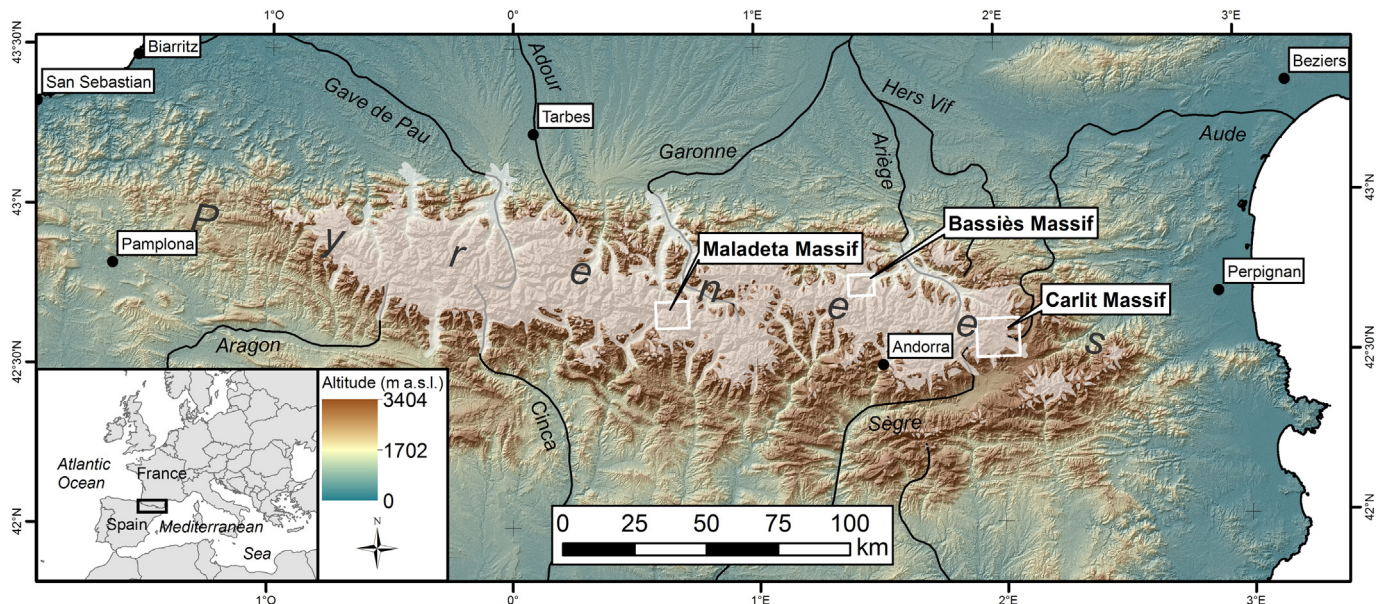


**Fig. 1.** Location map and icefield palaeogeography in the Pyrenees. White area: Würmian Maximum Icefield Extent after Calvet et al. (2011). White rectangles: study areas. Hillshading: ASTER GDEM v2, ground resolution: 30 m (NASA and METI). Projection: WGS84.

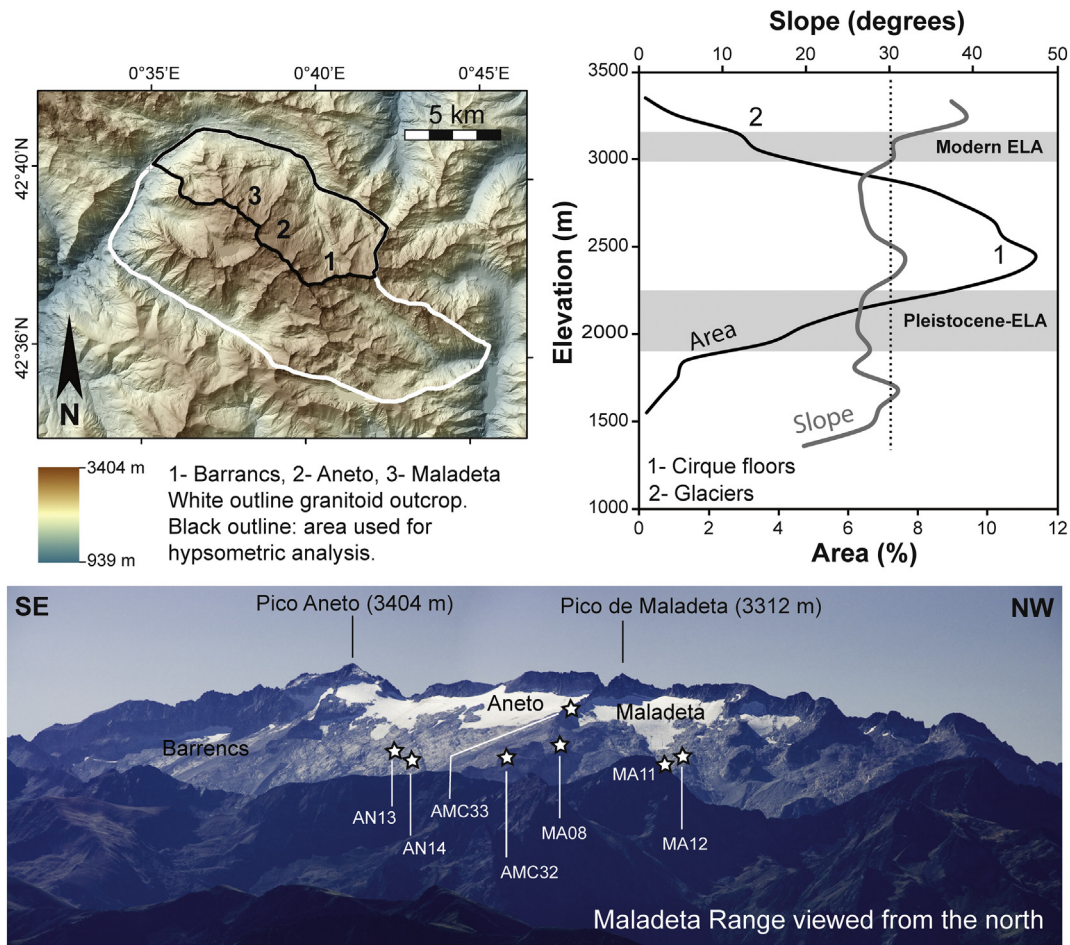


**Fig. 2.** Hypsometric features of the north side of the Maladeta Range. Digital elevation source: LiDAR PNOA®, ground resolution: 5 m, Instituto Geográfico Nacional.

undergoing NW–SE crustal extension, initially related to the opening of the western Mediterranean back-arc basin. At the end of the Oligocene and during the middle Miocene, a well-dated erosion surface bevelled parts of the Pyrenean structures, with vestiges best preserved in the eastern (Calvet, 1996; Calvet and Gunnell, 2008) and central parts of the range (Ortuño et al., 2008, 2013). Uplift and fragmentation of this paleic (i.e., preglacial; Goodfellow, 2007) erosion surface occurred during the last 10 Ma and is currently one of the first-order landscape features of the Pyrenees. Based on an assumption of continuous post-orogenic uplift since ~10 Ma (Gunnell et al., 2009; Ortuño et al., 2013), supported by rates of canyon incision in response to active crustal uplift (Calvet et al., 2015a), and based further on the position of the Pleistocene ELA inferred from cirque-floor altitudes (~1600 m on the north-facing mountain front and ~2000–2200 m on the south-facing mountain front; see Delmas et al., 2015), the Axial Zone by late Pliocene times had already attained altitudes compatible with the development of cirque glaciers. A systematic analysis of cirque morphometry throughout the eastern Pyrenees has nonetheless shown that the impact of Pleistocene glaciation varied substantially, depending on whether the ranges were situated at the core or at the periphery of the icefield (García-Ruiz et al., 2000; Delmas et al., 2014, 2015). The three ranges under investigation (Maladeta, Bassiès, and Carlit) were selected as a means of sampling the full spectrum of palaeoclimatic regimes and landform occurrences.

## 2.2. Pleistocene glacial impact on the landscape

The Maladeta range coincides with a Hercynian granite batholith. Its high elevation (3400 m) compensates its sheltered position from the influx of Atlantic weather systems and explains the ubiquitous imprint of

alpine glaciation. Sharp ridgetops, or arêtes, rise between a population of wide, often shallow *van*-shaped cirques (*van* is a French word for winnowing basket), with a few deeper variants containing lakes (Fig. 2). Small residual glaciers, mostly in north-facing cirques, have been undergoing rapid recession since the LIA.

The Bassiès range, also part of a granodiorite pluton, is directly exposed to the moisture-laden Westerlies entering the area from the Atlantic. This feature ensured abundant ice accumulation despite the comparatively low range-summit elevations (ca. 2600 m). The glacial morphology (*van* cirques) is in most ways identical to that of the Maladeta, with a small minority of ‘armchair’ cirques (flat to overdeepened floors with high headwalls) on the western margin of the range. The most conspicuous difference is the presence of wide and low-gradient ridgetops bearing thick vestiges of pre-Würmian (perhaps pre-Quaternary) bedrock weathering profiles and even larger vestiges of a paleic surface on the northern edge of the range (Fig. 3).

The southeastern half of the Carlit Range overlooks the intermontane Cerdagne Basin. It exhibits a more varied assortment of geological outcrops, with a granodiorite pluton and hornfels rim intruded into micashist and gneiss country-rock outcrops farther north. The effects of glaciation on the morphology of this elevated massif (2900 m) have been limited because of its situation in a drier, Mediterranean climatic zone and a relatively sheltered, south-facing environment. Glaciers above the Pleistocene ELA (2000–2200 m) formed widely spaced cirques around the southern edges of the paleic summit surface. Another unique feature is that the cirque floors connect with an extensive Cenozoic pediment ca. 1800–2300 m (e.g., Gunnell et al., 2009, Fig. 2a therein), which was unevenly scoured by plateau ice and cut by shallow glacial troughs (Fig. 4).

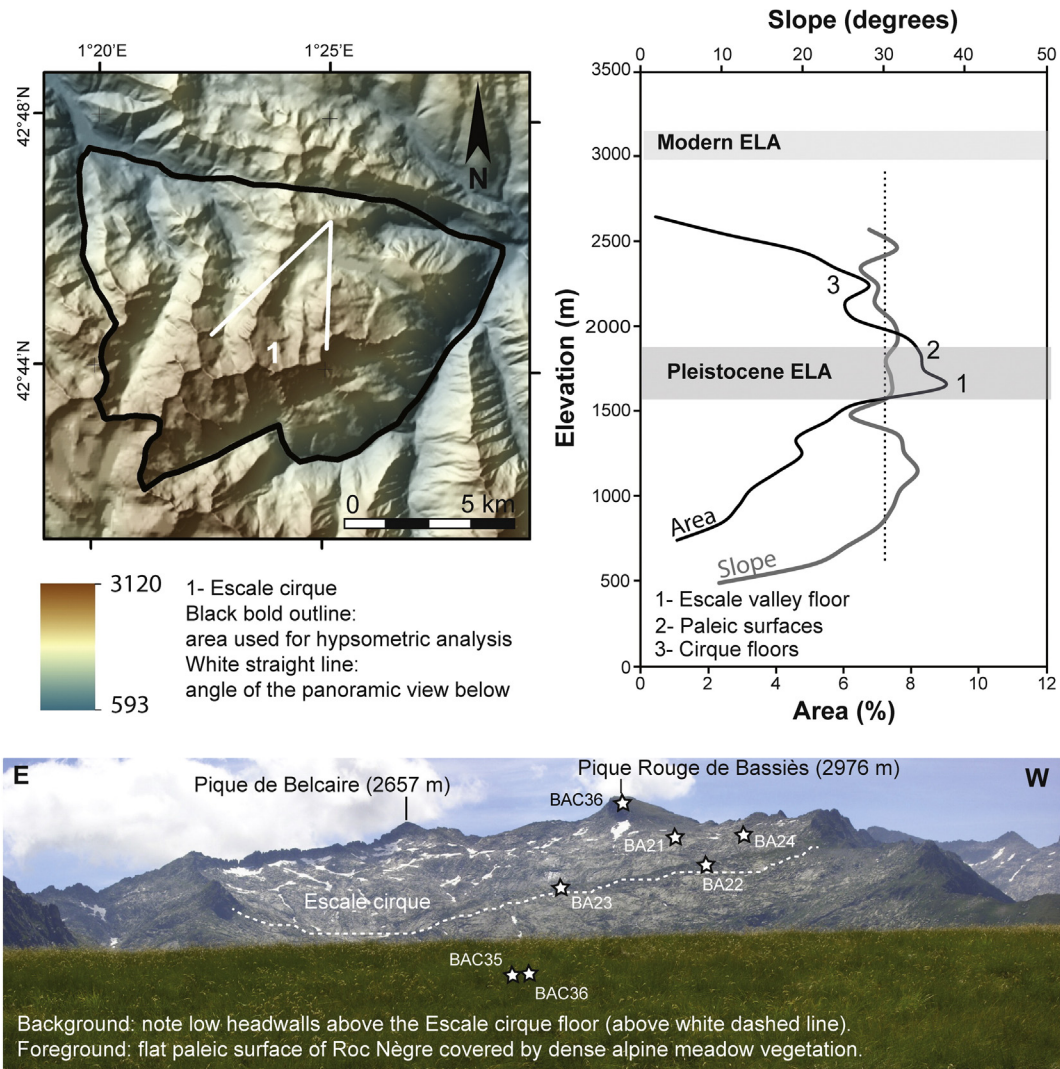


**Fig. 3.** Hypsometric features of the north side of the Bassiès Range. Digital elevation source: BD Alti ©, ground resolution: 25 m, Institut Géographique National.

### 2.3. Mountain-range hypsometry

The varying mix of glacial and nonglacial landscape components is detected in the hypsometric signatures of each mountain range (Figs. 2, 3, 4). Hypsometric analysis has been used as a tool for appreciating the impact of Quaternary glaciation on mountain landscapes (Brocklehurst and Whipple, 2004) and for determining the relationship between hypsometric maxima and former ELAs (e.g., Egholm et al., 2009; Robl et al., 2015b). The area–elevation curve of the Maladeta is unimodal and displays a broad hump ranging from just above the Pleistocene ELA to the cirque floors. In the other two ranges, the hypsometric curve is more sharply bimodal and reflects a weaker glacial impact. In the Bassiès, the main mode occurs exactly at the Pleistocene ELA but does not correspond to the shelf formed by the cirque floors. The latter occur around 2300–2400 m and define the secondary mode. The Carlit curve displays two modes of similar magnitude occurring just above and just below the Pleistocene ELA. However, neither of those two maxima are ascribable to the glacial geomorphology: they capture instead the presence of the extensive paleic pediment (or lower paleic surface), which rises progressively from elevations of ~1800 to ~2300 m below the girdle of cirques (Fig. 4). The slope–elevation curves (Figs. 2, 3, 4) complement and confirm these observations.

### 2.4. Cirque glaciation during the last termination and the Holocene

The chronology and paleogeography of the Pyrenean icefield are well established for the Würmian Maximum Icefield Extent (WMIE, Fig. 1; Calvet, 1996; Calvet et al., 2011), but the chronology and extent of cirque glaciation during the Last Termination (i.e., the time interval between the Global LGM and the beginning of the Holocene; Wohlfarth, 1996; Hoek, 2009; Denton et al., 2010) and the Holocene are poorly known (Delmas et al., 2015). In the Maladeta, the distribution of glacial deposits nonetheless has been mapped extensively and has provided a consistent relative chronostratigraphy (Fig. 5A). Martínez de Pósito (1989), García-Ruiz et al. (1992), and Copons and Bordonau (1997) distinguished four stades subsequent to the WMIE (known here as ‘Fase Inicial’, or Initial phase). (i) The first stade (‘Episodio de Glaciares de Valle de Altitud’, or elevated valley glacier phase) involved an 11-km-long valley glacier supplied by cirques in the Maladeta, Aneto, Barrencs and Escaleta and terminating at an elevation of ca. 1750 m. (ii) The second stade (‘Episodio de Glaciares de Circo de Altitud’, or elevated cirque glacier phase) was a period when the Maladeta and Escaleta cirque glaciers became disconnected. Their respective fronts stood between 2000 and 2100 m, just below the cirque floors. (iii) The third stade (‘Fase de Glaciares Rocosos’, or rock-glacier phase) actually

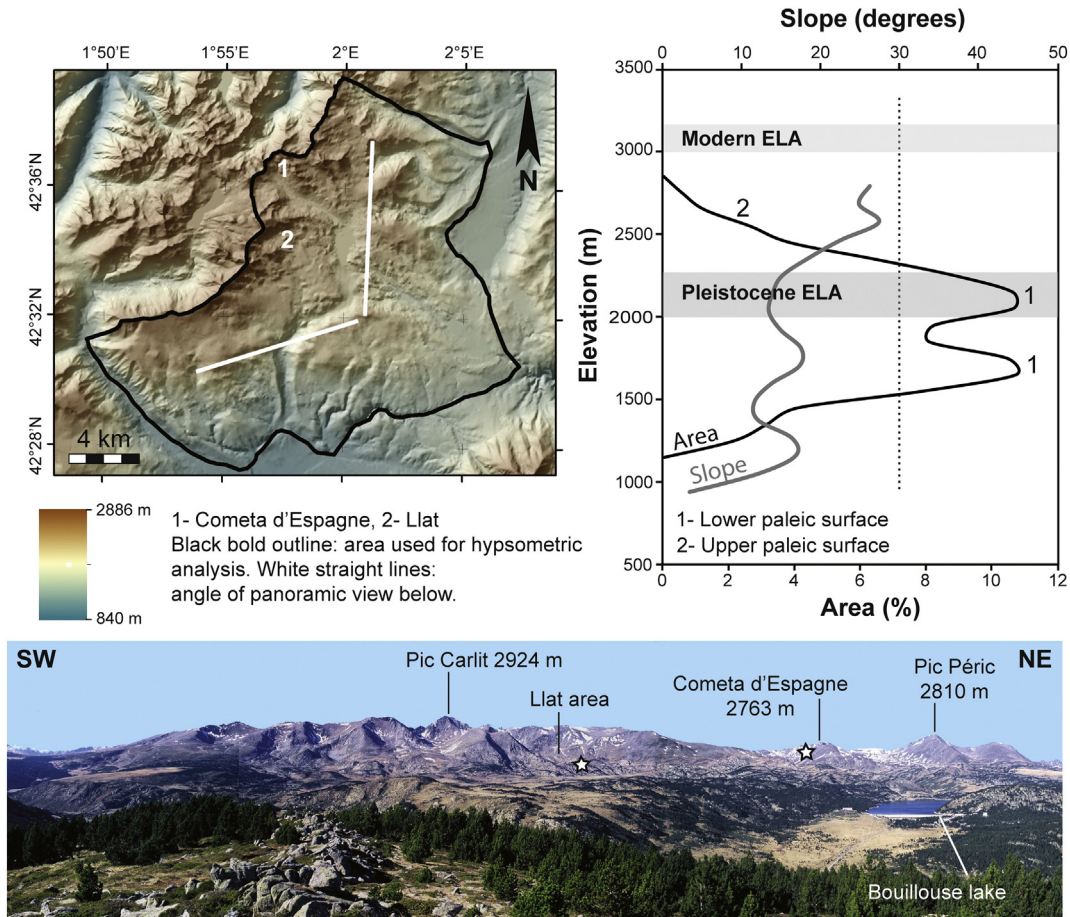


Fig. 4. Hypsometric features of the Carlit Range (south side). Digital elevation source: BD Alti ©, ground resolution: 25 m, Institut Géographique National.

includes a variety of deposits, e.g., rock glaciers but also ablation till depending on local, topographically controlled, climatic conditions where small residual glaciers persisted into the Holocene. In the elevated Maladeta range, the rock-glacier phase produced cirque glaciers terminating ca. 2200 m. None of these three stades have been dated, but they have been ascribed by default to the Last Termination by analogy with  $^{14}\text{C}$ -dated glacial deposit chronosequences obtained in other Pyrenean ranges (Copons and Bordonau, 1997). (iv) The fourth and final stade in the uppermost Esera valley is clearly ascribable to the LIA based on mid-nineteenth to early twentieth century photographic evidence (Copons and Bordonau, 1997; Chueca Cía et al., 2005; González Trueba et al., 2008; René, 2008, 2011, 2013). The LIA terminal moraines occur at elevations of 2300 m on the north and 2800 m on the south side of the range.

Previous work involving terrestrial cosmogenic nuclides (TCN) and  $^{14}\text{C}$  dating of glacial landforms and ice-marginal deposits has provided a consistent deglacial chronology of the Bassiès and SE Carlit (Delmas, 2005; Delmas et al., 2008, 2011, 2012; Figs. 6A, 7A). In both cases, the WMIE occurred during Marine Isotope Stage 4 (MIS 4). During MIS 3, the outlet glacier ice fronts underwent fluctuations in excess of 10 km in the Ariège valley, and over unknown distances in the Carlit. The last maximum icefield advance coincided with the Global LGM, was comparable to the MIS 4 icefield extent in the SE Carlit, but fell short of the MIS 4 ice position by ~7 km in the Ariège valley. Whether in the Ariège or the Carlit, the Global LGM ended in a rapid debacle, with the icefield retreating to the cirques as early as ~20–19 ka. During the Oldest Dryas (i.e., GS-2.1a following the Greenland isotope chronostratigraphy of Rasmussen et al., 2014), the icefield expanded once again; but its precise limits have only been constrained for the Carlit, where a 6-km-long

glacier filled the Grave U-shaped valley and spilled over onto the adjacent paleic pediment (Llat moraine, Fig. 7A).

No data exist for the Bassiès Range, but the neighbouring Trois-Seigneurs massif generated an ~5-km-long glacier in the Suc valley (Fig. 6A). During the Bølling–Allerød interstade (GI-1), the treeline rose to ~1700 m in the Ariège catchment (Reille and Andrieu, 1993) and the regional ELA to ~2700 m (Delmas et al., 2011, 2012). Given the limited elevation of the Bassiès and Carlit in comparison to the Maladeta, it is therefore likely that the Bølling–Allerød interstade resulted in glacier extinction—except perhaps for residual cirque glaciers in topographically suitable local settings. During the Younger Dryas (GS-1), a large number of Pyrenean cirques became deglaciated and populated by rock glaciers, e.g., in the SE Carlit (Fig. 7A). By inference, cirques lacking rock glaciers may have hosted small cirque glaciers during the Younger Dryas. This can be observed in the Carlit below the Cometa d'Espagne peak, where the presence of a cirque glacier during the Younger Dryas (GS-1a) has been confirmed by TCN dating of moraines (Delmas et al., 2008; Delmas et al., 2009). This finding is consistent with palaeoenvironmental data indicating that the treeline in the Ariège catchment descended to ~1300 m during the Younger Dryas (Reille and Andrieu, 1993). So did, by inference, the regional ELA.

### 3. Methods

#### 3.1. TCN sampling strategy

The collection of 36 samples for TCN analysis (Supplementary Table 1) focused on three kinds of rock surface. (i) Erratic boulders on the ridgetops of lateral and frontal moraines resting on, or immediately

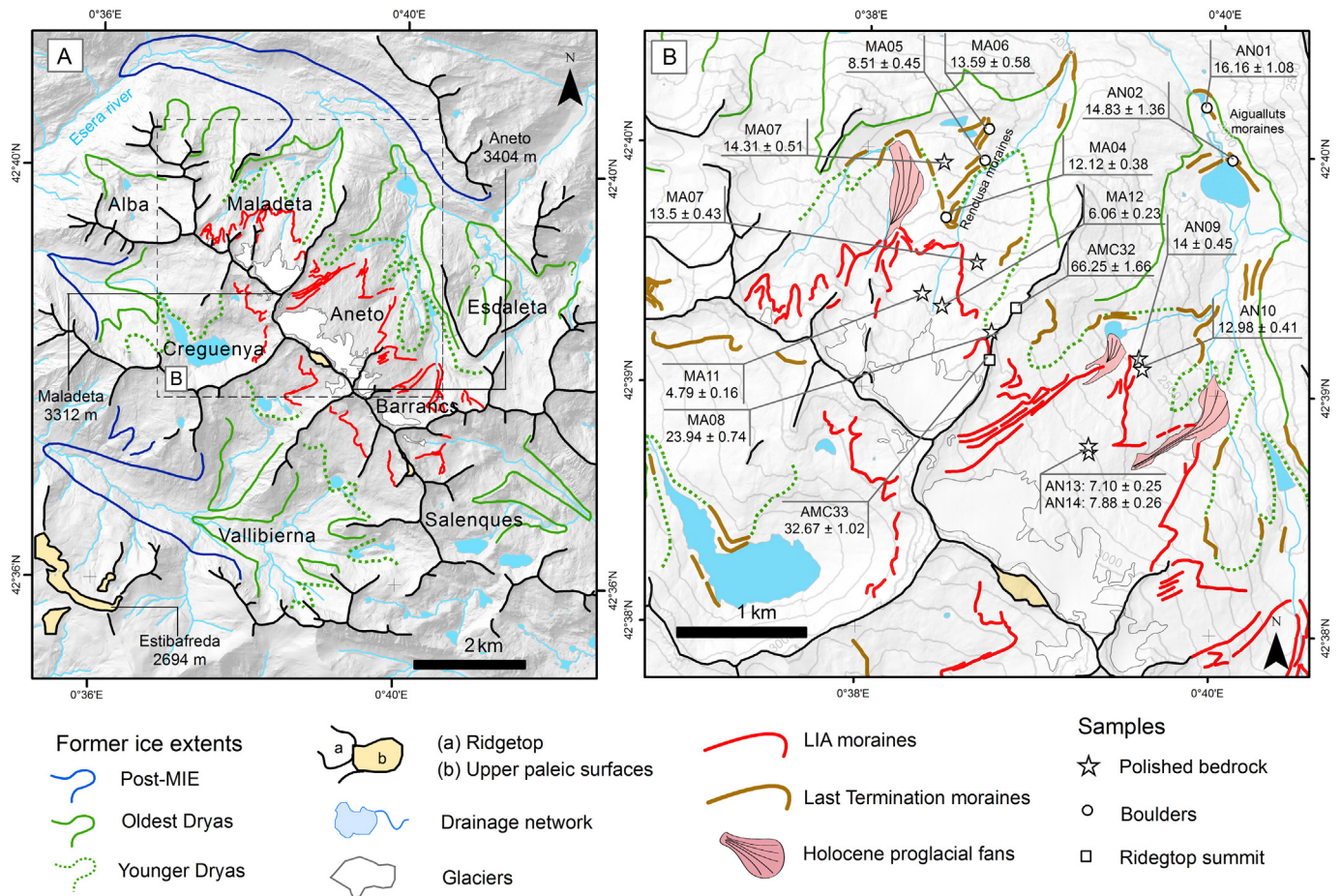


**Fig. 5.** Palaeogeography and chronology of cirque glaciation in the Maladeta Range. (A) Extent of the glacial advances subsequent to the WMIE (modified and completed from Copons and Bordonau, 1997). (B) Distribution of glacial deposits and cosmogenic nuclide samples in the Maladeta and Aneto cirques.

downvalley from, the cirque floors. Ideally, such samples date the time of moraine abandonment by a receding glacier. In the Maladeta, the TCN-dated moraines (Aigualluts and Renclusa, Fig. 5B) belong to the ‘Episodio de Glaciares de Circo de Altitud’ and ‘Fase de Glaciares Rocosos’ of Copons and Bordonau (1997). In the Bassiès, landform mapping and paleogeographic reconstructions are previously unpublished and document two glacial stades displaying datable lateral moraines at Legunabens and Mouscadou (Fig. 6B). For the Carlit, sample locations are shown in Fig. 7 and complement the collection of exposure ages previously presented in Delmas et al. (2008). In all cases, TCN samples were collected from the top surfaces of large boulders (1 to 5 m long) displaying clear signatures of englacial transport (boulders showing exfoliation or other pre- or postdepositional weathering features were avoided) in accordance with the principles used by Delmas et al. (2008) in the Carlit range, where the Würmian deglacial chronology has already been established (Fig. 7B). Boulders still partly embedded in finer matrix were preferred in order to minimize the risk of recent exhumation or gravitational displacement on the moraine flank (Putkonen and Swanson, 2003; Putkonen et al., 2008; Heyman et al., 2011). (ii) Ice-polished rock surfaces were sampled on stoss-and-lee landforms located on cirque floors situated in- and outboard of moraines dated as part of step (i). (iii) Bedrock surfaces on adjacent supraglacial ridgetops. These ridgetop sampling sites covered two settings typical of the area: arête-like ridgetops (AMC32, AMC33, and BAC 34, all collected from an area severely affected by frost cracking); and avenue-width, planar ridgetops (BAC35 and BAC36), which are vestiges of a paleic surface and are still covered by thick, in situ granitic saprolite.

### 3.2. Analytical procedure

Ridgetop bedrock samples underwent  $^{10}\text{Be}$  and  $^{26}\text{Al}$  measurements in view of detecting whether or not ridgetop denudation attained a steady state, but samples from erratic boulders and cirque-floor bedrock exposures were restricted to the production of  $^{10}\text{Be}$  inventories. The chemical procedure for  $^{10}\text{Be}$  and  $^{26}\text{Al}$  extraction from the rock samples was adapted by Braucher et al. (2011) from Brown et al. (1991) and Mercher and Herpers (1999). The samples were first crushed and sieved to obtain 250–1000  $\mu\text{m}$  rock particles, from which magnetic grains were removed using a magnetic separator. Chemical processing consisted of a sequence of dissolution steps using HCl and  $\text{H}_2\text{SiF}_6$  to eliminate all non-quartz materials, followed by another sequence of dissolution steps using diluted HF to remove the atmospheric  $^{10}\text{Be}$ . Following chemical dissolution,  $\sim 0.1$  g of an ASTER in-house  $^9\text{Be}$  carrier solution ( $(3.025 \pm 0.009) \times 10^{-3}$  g  $^9\text{Be}/\text{g}$  solution; Braucher et al., 2011) originating from deep-mined phenakite (Mercher et al., 2008) was added to the purified quartz. The measurement of stable  $^{27}\text{Al}$  intrinsically present in the samples was achieved using liquid aliquots analyzed by inductively coupled plasma optical emission spectrometry (ICP-OES) on an ICP6500 Thermo Scientific unit. After total dissolution of purified quartz using diluted HF solution and several solvent extractions,  $\text{Be}(\text{OH})_2$  and  $\text{Al}(\text{OH})_3$  were precipitated and then oxidized at 800 °C for 1 h. Powdered forms of the resulting BeO and  $\text{Al}_2\text{O}_3$  oxides, respectively, were then mixed with niobium powder and placed into cathodes for analysis using accelerator mass spectrometry (AMS). The AMS measurements of  $^{10}\text{Be}$  and  $^{26}\text{Al}$  concentrations were performed at the AMS

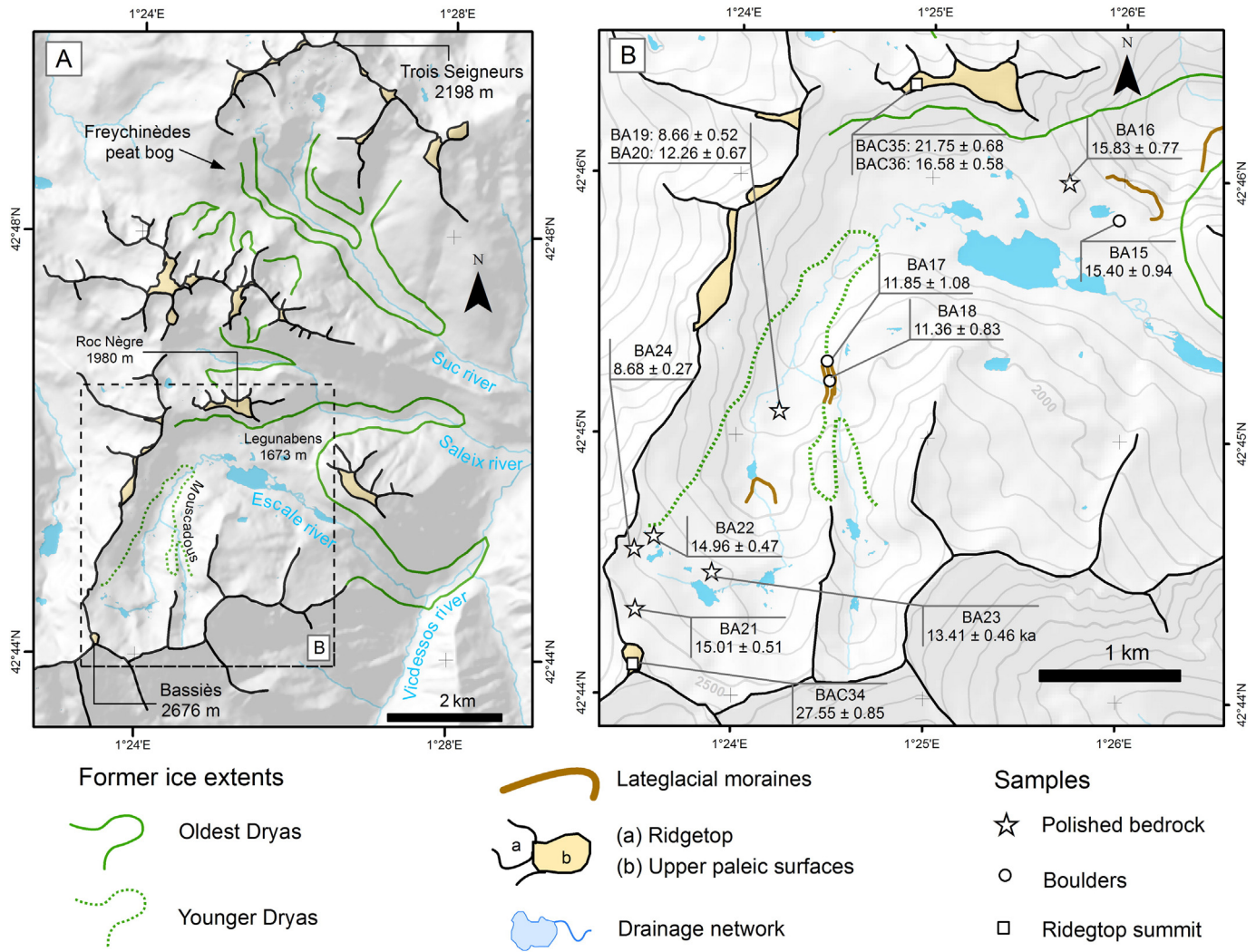


**Fig. 6.** Palaeogeography and chronology of cirque glaciations in the Bassiès Range. (A) Extent of glacial advances in the western part of the upper Vicdessos catchment during the Last Termination (source: Delmas et al., 2011, modified and completed). (B) Distribution of glacial deposits and cosmogenic nuclide samples in the Escalè cirque.

National Facility ASTER, located at the CEREGE in Aix-en-Provence, France (Arnold et al., 2010). The  $^{10}\text{Be}/^9\text{Be}$  ratios were calibrated directly against the National Institute of Standards and Technology standard reference material NIST SRM 4325 using an assigned  $^{10}\text{Be}/^9\text{Be}$  value of  $(2.79 \pm 0.03) \times 10^{-11}$  (Nishiizumi et al., 2007) and a  $^{10}\text{Be}$  half-life of  $1.387 \pm 0.012$  Ma (Chmeleff et al., 2010; Korschinek et al., 2010). The  $^{26}\text{Al}/^{27}\text{Al}$  ratios were measured against the ASTER in-house standard SM-Al-11, whose  $^{26}\text{Al}/^{27}\text{Al}$  ratio of  $(7.401 \pm 0.064) \times 10^{-12}$  has been cross-calibrated (Arnold et al., 2010) against primary standards in the context of a round-robin exercise (Merchel and Bremser, 2004). The  $^{26}\text{Al}$  half-life reported in this study is  $0.717 \pm 0.017$  Ma (Samworth et al., 1972). The  $^{26}\text{Al}/^{10}\text{Be}$  production ratio resulting from the standardization method used at ASTER (SM-Al-11/07KNSTD) is  $\sim 6.61 \pm 0.52$ . This value is based on the ratio originally determined by Nishiizumi et al. (2007). Surface production rates were scaled using the Stone (2000) polynomial with a sea-level high-latitude (SLHL) production rate of  $\sim 4.02$  at/g/a for  $^{10}\text{Be}$ . Corrections for topographic shielding and sample geometry were derived from Dunne et al. (1999). Corrections for mass shielding were calculated using the equation of Dunai (2010). Correction factors for snow shielding were calculated using the equation of Gosse and Phillips (2001) with a mean value for snow density of  $0.25$  g/cm $^3$ ; (Supplementary Table 1).

### 3.3. TCN modelling strategy on moraine boulders and ice-scoured cirque-floor surfaces

Exposure times and denudation rates produced in this study were calculated using the following equation (Braucher et al., 2011):

$$\begin{aligned}
 N(x, \varepsilon, t) = & N_{\text{inherited}} \exp(-\lambda t) \\
 & + \frac{P_{\text{sp}} \cdot \exp\left(-\frac{x}{L_n}\right) \left(1 - \exp\left(-t\left(\frac{\varepsilon}{L_n} + \lambda\right)\right)\right)}{\frac{\varepsilon}{L_n} + \lambda} \\
 & + \frac{P_{\text{slow}} \cdot \exp\left(-\frac{x}{L_{\text{slow}}}\right) \left(1 - \exp\left(-t\left(\frac{\varepsilon}{L_{\text{slow}}} + \lambda\right)\right)\right)}{\frac{\varepsilon}{L_{\text{slow}}} + \lambda} \\
 & + \frac{P_{\text{fast}} \cdot \exp\left(-\frac{x}{L_{\text{fast}}}\right) \left(1 - \exp\left(-t\left(\frac{\varepsilon}{L_{\text{fast}}} + \lambda\right)\right)\right)}{\frac{\varepsilon}{L_{\text{fast}}} + \lambda}
 \end{aligned} \tag{1}$$

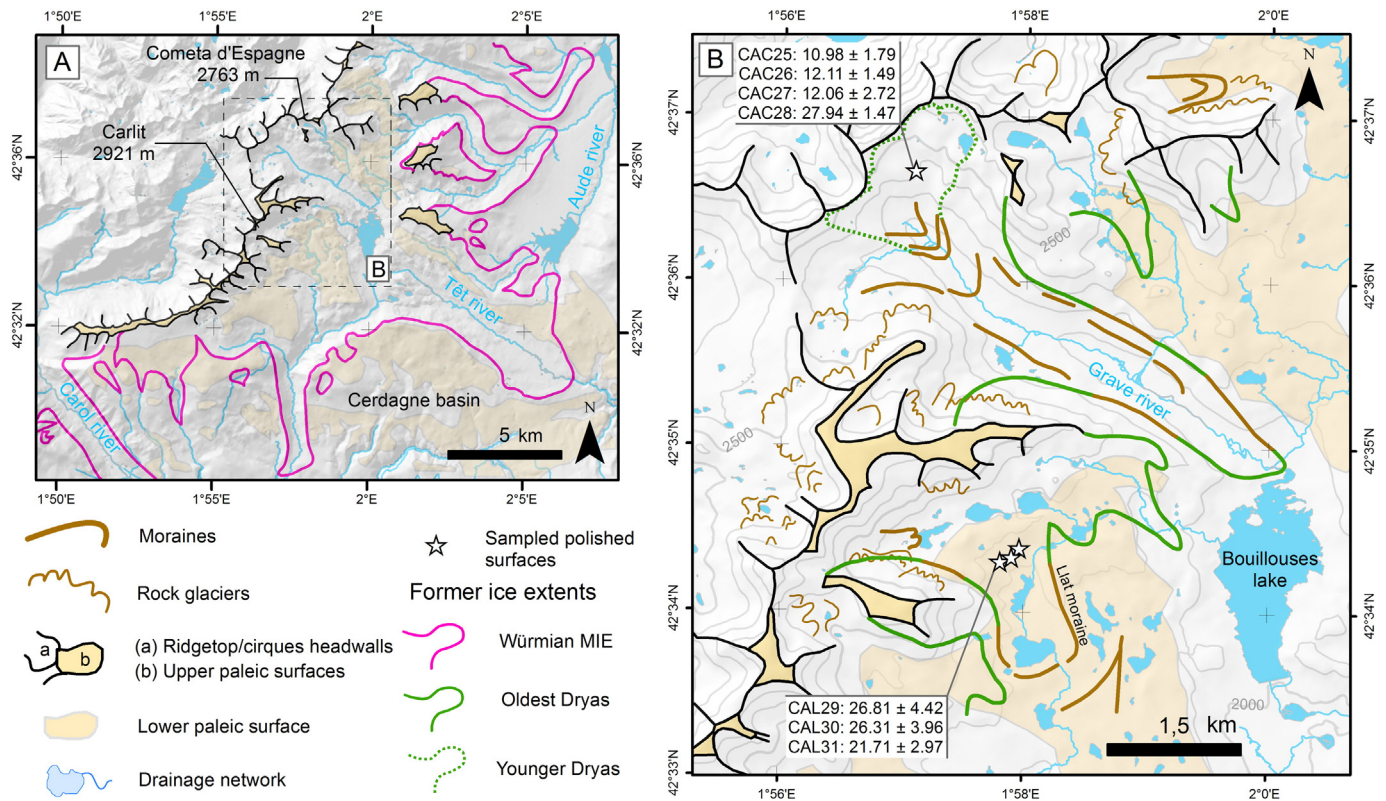


**Fig. 7.** Palaeogeography and chronology of cirque glaciations in the Carlit Range. (A) Würmian icefield palaeogeography on the south side of the Carlit Range (after Delmas et al., 2008). (B) Distribution of glacial deposits and cosmogenic nuclide samples in the Llat and Cometa d'Espagne cirques.

where  $N(x, \varepsilon, t)$  is the nuclide concentration as a function of distance  $x$  (typically expressed as a function of depth  $z$ , cm, and bedrock density  $\rho$ , g/cm<sup>3</sup>), denudation rate  $\varepsilon$  (g/cm<sup>2</sup>/a), and exposure time  $t$  (years). The  $P_{sp}$ ,  $P_{\mu slow}$ ,  $P_{\mu fast}$ , and  $L_{sp}$  (160 g/cm<sup>2</sup>),  $L_{\mu slow}$  (1500 g/cm<sup>2</sup>), and  $L_{\mu fast}$  (4320 g/cm<sup>2</sup>) are the production rates and attenuation lengths of neutrons, slow muons and fast muons, respectively;  $\lambda$  is the radioactive decay constant of the TCN under investigation;  $N_{inherited}$  is the <sup>10</sup>Be concentration acquired during windows of exposure time prior to subglacial denudation. This <sup>10</sup>Be remains preserved in the sample in situations where glacial denudation has failed to strip away the TCN-pervaded bedrock and thereby reset the TCN clock.

### 3.3.1. Minimum exposure ages

The <sup>10</sup>Be concentrations measured on boulders and cirque-floor bedrock steps were first converted to minimum exposure ages (MEAs) using Eq. (1) while assuming no postglacial surface denudation and no preglacial nuclide inheritance (Table 1). On that basis, and given the precautions taken in selecting surface samples (Section 3.1), the MEAs obtained from boulders were interpreted as moraine depositional ages, thus providing baseline information about the ice fluctuation chronology in each cirque. Even when boulder surfaces have suffered some postdepositional denudation, as long as postglacial denudation rates are less than a few dozen mm/ka, losses can be ignored provided exposure times did not exceed ~20 ka (Gunnell et al., 2013). In the case of these late Würmian or younger moraines, therefore, the exposure ages are expected to be accurate. Additional controls on the cirque-glacier chronology were provided by correlations with regional palaeoenvironmental data gained from the literature and by tuning of age results to the palaeotemperature chronostratigraphy provided by Greenland ice cores (Rasmussen et al., 2014).

The MEAs on polished bedrock-step surfaces were used as tools for detecting whether or not subglacial bedrock denudation on cirque floors was sufficiently deep to reset TCN inventories inherited from periods of preglacial exposure. Discrepancies between a cirque-floor MEA

and the ages of adjacent moraines provide options for determining the contribution from preglacial nuclide inheritance to the measured bedrock MEA. Accordingly, because TCN accumulation on cirque floors occurs between periods of bedrock stripping and shielding by glaciers, the MEAs obtained on cirque floors will fit into three ideal scenarios: (i) when the MEAs on polished bedrock are consistent with the age of the nearest moraine situated outboard of the sampling site, we can infer that the depth,  $z$ , of stripped bedrock at the sampling point during the last subglacial burial event was sufficiently large to reset the TCN clock (i.e., to erase any TCN concentrations inherited from a preglacial exposure history); (ii) when the MEAs are younger than the adjacent glacial moraines, we can infer that some till deposits originally shielding the bedrock surface were removed by nonglacial processes only some time after glacier recession; (iii) when the MEAs are older than the adjacent glacial moraines, we can infer that some component (known as nuclide inheritance,  $N_{inherited}$  in Eq. (1)) of the TCN inventory was carried over from a period preceding the last subglacial burial cycle; i.e., subglacial denudation failed to reset the TCN clock. Scenario (iii) is upsetting for geochronological purposes because the exposure ages do not directly document a palaeoclimatic event, but it is useful to geomorphologists because the anomaly can serve as a proxy for inferring subglacial denudation rates. The following section explains how.

### 3.3.2. Inherited TCN concentrations as proxies for calculating depths of subglacially denuded bedrock

We proceeded to extract additional information from inherited <sup>10</sup>Be components that cause cirque-floor MEAs to be greater than the exposure ages obtained for the adjacent moraines. The principles of the procedure are illustrated in Fig. 8. Given the attenuation lengths of <sup>10</sup>Be in crystalline bedrock, the presence of excess TCN in a granite sample typically implies that denudation was < ~3 m during the last subglacial burial event (Fabel et al., 2002; Marquette et al., 2004; Briner et al., 2005a, 2005b; Phillips et al., 2006; Li et al., 2008).

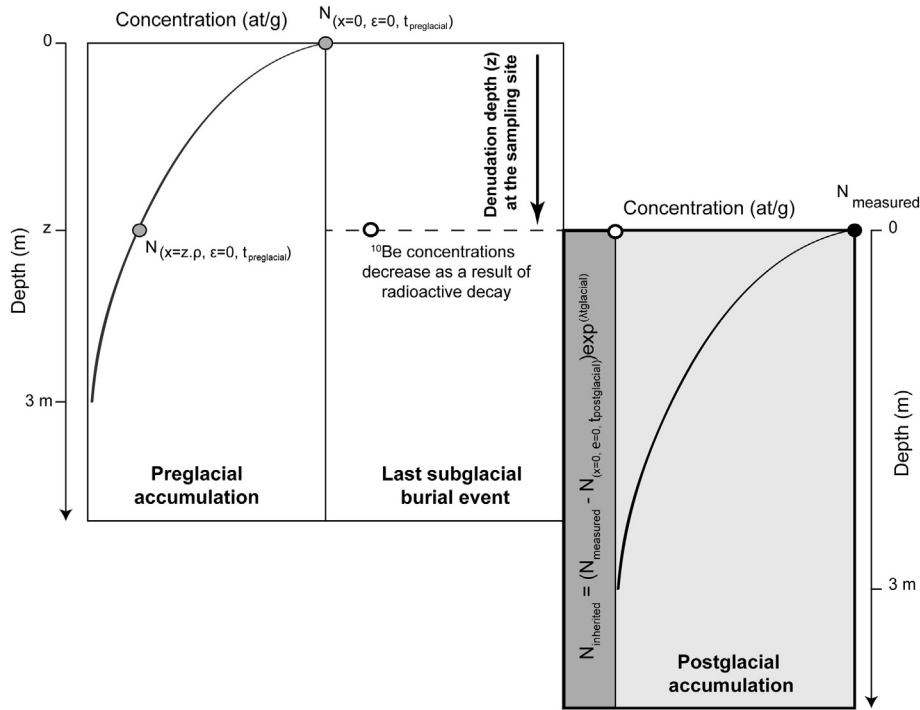


**Fig. 8.** Scenario of a surface-exposure history leading to the presence of inherited nuclides on a glaciated bedrock surface. The relevant example here is an ice-scoured whaleback on a cirque floor.

The inherited  $^{10}\text{Be}$  component was produced at some depth  $z$  at a time when the sample was exposed to cosmic rays because it was situated within the  $^{10}\text{Be}$  accumulation zone (i.e.,  $0 \leq z \leq 3$  m) and not shielded by a glacier. Conditions such as these were prevalent at the sampling sites during interglacial or interstadial periods (defined as  $t_{\text{preglacial}}$ ). While subsequently covered by the glacier, the bedrock was eroded down to depth  $z$ , where it became reexposed after glacier recession and thus available for sample collection at the surface. The first step toward obtaining  $z$  involves calculating the sample MEA while assuming no inheritance (i.e., by holding  $N_{\text{inherited}} = 0$ ). When the sample's MEA

exceeds the duration of exposure after glacier recession (defined as  $t_{\text{postglacial}}$ ),  $N_{\text{inherited}}$  can be calculated from Eq. (1) as:

$$N_{\text{inherited}} = \left( N_{\text{measured}} - N_{(x=0, \epsilon=0, t_{\text{postglacial}})} \right) \exp(\lambda t_{\text{glacial}}) \quad (2)$$

Subsequently using Eq. (1), and assuming that the sample was not exposed before  $t_{\text{preglacial}}$ , obtaining the value of  $z$  becomes possible (with  $t = t_{\text{preglacial}}$  and assuming no denudation during that time window). Given the measured nuclide concentration of the sample

**Table 2**  
Würmian cirque-floor denudation rates inferred from apparent exposure ages corrected for TCN inheritance.

Sample ID	Concentration ( $10^4$ at/g)	MEA (ka $\pm$ $1\sigma$ )	$N_{\text{inherited}}$ ( $\times 10^4$ at/g)		Denudation depth ( $z$ , cm) <sup>a</sup>		Subglacial denudation rates (mm/ka) <sup>a</sup>	
			min	max	min	max	min	max
Scenario: the last glacial shielding event occurred during the Younger Dryas ( $t_{\text{postglacial}} = 13.5$ ka, $t_{\text{preglacial}} = 15$ ka, $t_{\text{glacial}} = 100$ ka)								
MA07	33.14 $\pm$ 1.05	13.50 $\pm$ 0.43	reset	1.12	216	~300–400	21.6	~30–40
MA08	66.42 $\pm$ 2.05	23.94 $\pm$ 0.74	33.73	38.85	18	26	1.8	2.6
AN09	33.08 $\pm$ 1.05	14.00 $\pm$ 0.45	0.13	2.30	194	~300–400	19.4	~30–40
AN10	30.31 $\pm$ 0.95	12.98 $\pm$ 0.41	reset	reset	>300	>300	>30	>30
BA21	35.75 $\pm$ 1.21	15.01 $\pm$ 0.51	2.39	4.81	120	193	12.0	19.3
BA22	33.06 $\pm$ 1.04	14.96 $\pm$ 0.47	2.20	4.29	119	191	11.9	19.1
BA23	28.74 $\pm$ 0.98	13.41 $\pm$ 0.46	reset	0.89	216	~300–400	21.6	~30–40
CAC25	23.64 $\pm$ 3.85	10.98 $\pm$ 1.79	reset	reset	>300	>300	>30	>30
CAC26	22.33 $\pm$ 2.75	12.11 $\pm$ 1.49	reset	0.20	>300	>300	>30	>30
CAC27	28.08 $\pm$ 6.33	12.06 $\pm$ 2.72	reset	2.99	183	~300–400	18.3	~30–40
CAC28	63.73 $\pm$ 3.34	27.94 $\pm$ 1.47	29.70	36.39	0	9	0	0.9
Scenario: the last glacial shielding event occurred during the Oldest Dryas ( $t_{\text{postglacial}} = 14.7$ ka, $t_{\text{preglacial}} = 15$ ka, $t_{\text{glacial}} = 100$ ka)								
MA03	33.2 $\pm$ 1.18	14.31 $\pm$ 0.51	reset	reset	>300	>300	>30	>30
Scenario: the last glacial shielding event occurred during the Oldest Dryas ( $t_{\text{postglacial}} = 17.2$ ka, $t_{\text{preglacial}} = 15$ ka, $t_{\text{glacial}} = 100$ ka)								
CAL29	58.37 $\pm$ 9.63	26.54 $\pm$ 4.38	11.79	31.08	3	62	0.3	6.2
CAL30	57.67 $\pm$ 8.68	26.18 $\pm$ 3.94	11.79	29.18	7	63	0.7	6.3
CAL31	47.63 $\pm$ 6.52	21.71 $\pm$ 2.97	3.84	16.92	40	129	4.0	12.9

<sup>a</sup> Calculation of denudation rates takes account of neutron- and muon-derived  $^{10}\text{Be}$  production, of correction coefficients for topography, snow cover, and is based on Eq. (2). Bedrock density is  $2.65 \text{ g/cm}^3$ .

( $N_{measured}$ ), the duration of shielding by the glacier ( $t_{glacial}$ ), and the value of  $z$ , the denudation rate is  $z/t_{glacial}$ . This procedure presupposes a well-constrained deglaciation chronology and was applied for different durations of  $t_{glacial}$  on the basis of moraine ages and other independent constraints (Fig. 8, Tables 2 and 3).

### 3.4. TCN modelling strategy on supraglacial ridgetops

The  $^{10}\text{Be}$  concentrations measured on supraglacial ridgetops (Table 4) were also converted to MEAs from Eq. (1) under an analytical assumption of no postglacial denudation and no preglacial nuclide inheritance in order to compare results with exposure ages on cirque floors as a geologically improbable but useful starting point (Table 1). The  $^{10}\text{Be}$  concentrations were also converted into maximum denudation rates by using Eq. (1) while assuming that TCN concentrations had reached a steady state (i.e.,  $^{10}\text{Be}$  production and  $^{10}\text{Be}$  loss through denudation and radioactive decay define an equilibrium). The  $^{26}\text{Al}/^{10}\text{Be}$  ratio provides a check on whether the samples recorded continuous rather than intermittent exposure and whether exposure times were sufficiently long for the assumed steady state to have been attained (value of  $t$  set to infinity in Eq. (1)). The time needed to attain nuclide steady state under a specific denudation regime is the integration time (Lal, 1991). The greater the denudation rate, and likewise the shorter a nuclide's half-life, the shorter the integration time. Consequently, the secular equilibrium concentration is reached faster by  $^{26}\text{Al}$  than by  $^{10}\text{Be}$ . The integration time thus also indicates the geological time window over which denudation rates obtained from Eq. (1) are relevant and is calculated as:

$$\text{Integration time} = \frac{1}{\lambda + \frac{\varepsilon}{\Lambda}} \quad (3)$$

where  $\lambda$  is the disintegration constant ( $\text{a}^{-1}$ ),  $\Lambda$  is the attenuation length ( $\text{g}/\text{cm}^2$ ), and  $\varepsilon$  the denudation rate ( $\text{g}/\text{cm}^2/\text{a}$ ). In a context where exposure times do not exceed  $\sim 20$  ka, the integration time calculated on the basis of one attenuation length in Eq. (3) is close to the MEA calculated from Eq. (1) when assuming no postglacial surface denudation and no preglacial nuclide inheritance.

## 4. Results

### 4.1. Apparent exposure ages on moraines and cirque floors

Paired comparisons between boulder and bedrock-step MEAs (Table 1) provide a criterion for distinguishing between samples suitable for dating the ice-fluctuation chronology in the cirque zone (population of samples with no TCN inheritance) from samples usable as indicators of cirque-floor glacial denudation rates (population of samples displaying TCN inheritance).

#### 4.1.1. Aneto and Maladeta

The MEAs from moraine ridgetops and ice-scoured bedrock steps in the Aneto and Maladeta cirques correspond to sites situated among the three younger glacial stades reported by Copons and Bordonau (1997): the 'Elevated cirque glacier phase' (Aigualluts moraines), the 'Rock-glacier phase' (Renclusa moraines), and the LIA (Fig. 5B, Table 1). Samples AN01 and AN02 yielded MEAs of  $16.2 \pm 1.1$  and  $14.8 \pm 1.4$  ka, respectively, indicating that the two Aigualluts moraines were constructed during the Oldest Dryas (GS-2.1a). A polished bedrock step (MA03) located inboard of the Aigualluts glacial stade but outboard of the Renclusa moraine yielded an age of  $14.3 \pm 0.5$  ka. At this time, the Maladeta and Escaleta cirque glaciers were no longer connected to the 5-km-long Aneto–Barrancs glacier (Fig. 5A), which reached the 2000-m elevation contour (position of the Aigualluts frontal moraines). The Maladeta glacier front was probably located at a similar elevation, whereas the Escaleta glacier front may have reached the 2170-m contour. The MA03 MEA indicates that this area became definitively ice-free at the beginning of the Bølling–Allerød interstadial (GI-1), in good agreement with regional paleoenvironmental data (Reille and Andrieu, 1993; Millet et al., 2012) and the Greenland records (Rasmussen et al., 2014).

The Renclusa system consists of a succession of three lateral moraines (Fig. 5B) connecting to a bedrock spur that was ice-covered during the Aigualluts stade (Oldest Dryas, GS-2.1a). The outermost moraine (MA06:  $13.6 \pm 0.6$  ka) formed during the Older Dryas (GI-1d), whereas the innermost moraine (MA04:  $12.1 \pm 0.4$  ka) formed during the Younger Dryas (GS-1). The boulder on the intermediate moraine (MA05) provided an MEA of  $8.5 \pm 0.4$  ka. This anomalously young exposure age likely results from a late exhumation of the boulder out of its till matrix, a process perhaps promoted by undercutting of the moraine by proglacial streams during the Holocene. The absence of moraine accumulations between the innermost Renclusa and the LIA moraines strongly suggests that the historical LIA ice front is indistinguishable from any earlier maximum Holocene ice fronts – an inference consistent with recent overviews of the European Neoglacial in the Alps and Norway (Matthews, 2013) and more widely across the Northern hemisphere (Solomina et al., 2015). The bedrock surfaces between the Renclusa and the LIA moraines have consequently undergone continuous exposure since the end of the Younger Dryas (GS-1). The voluminous ablation till deposits contained in the LIA moraine can be ascribed to an unspecified number of Holocene glacial readvances.

Two bedrock steps were sampled on the Maladeta cirque floor between the innermost Renclusa and the LIA moraines (Fig. 5B). Sample MA07 ( $13.5 \pm 0.4$  ka) is located in the central part of the Maladeta cirque floor, in the path of the main ice stream; whereas MA08 ( $23.9 \pm 0.7$  ka) lies on the margin of the cirque floor, immediately at the foot of the LIA lateral moraine, near a large diffluence breach in the ridgetop. In both cases, the MEAs are obviously older than the last deglaciation of the ice-polished surfaces, which occurred (as mentioned above) immediately after the Younger Dryas (GS-1) glacial readvance

**Table 3**  
Cirque-floor denudation rates during the Last Termination.

Sample ID	Concentration ( $\times 10^4$ at/g)	MEA (ka $\pm 1\sigma$ )	$N_{inherited}$ ( $\times 10^4$ at/g)		Bedrock denudation depth (z, cm) <sup>a</sup>		Subglacial denudation rates (mm/ka) <sup>a</sup>	
			min	max	min	max	min	max
Scenario 1: cirque glaciation occurred during the Younger Dryas readvance ( $t_{postglacial} = 11.7$ ka, $t_{preglacial} = 1.8$ ka, $t_{glacial} = 1.2$ ka)								
AN10	$30.31 \pm 0.95$	$12.98 \pm 0.41$	2.10	4.05	4	44	33	366
CAC25	$23.64 \pm 3.85$	$10.98 \pm 1.79$	reset	2.30	32	>300	267	>2500
Scenario 2: cirque glaciation occurred during the Late Holocene readvance ( $N_{inherited} = N_{measured}$ , $t_{preglacial} = 8.4$ ka, $t_{glacial} = 3.3$ ka)								
MA11	$12.78 \pm 0.81$	$4.79 \pm 0.16$	13.24	14.15	32	36	97	109
MA12	$16.43 \pm 1.05$	$6.06 \pm 0.23$	16.92	18.27	17	22	52	67
AN13	$19.43 \pm 1.04$	$7.1 \pm 0.25$	20.09	21.54	8	12	24	36
AN14	$21.51 \pm 1.07$	$7.88 \pm 0.26$	22.29	23.80	2	6	6	19

<sup>a</sup> Calculation of denudation rates takes account of neutron- and muon-derived  $^{10}\text{Be}$  production, of correction coefficients for topography and snow cover, and is based on Eq. (2). Bedrock density is  $2.65 \text{ g}/\text{cm}^3$ .

**Table 4**  
 $^{10}\text{Be}$  and  $^{26}\text{Al}$  cosmogenic nuclide data and denudation rates on supraglacial ridgetops.

Sample ID	Concentration ( $\times 10^4$ at/g $\pm 1\sigma$ ) $^{10}\text{Be}$	Integration time (ka)				Denudation rate <sup>a</sup> (mm/ka $\pm 1\sigma$ )		$^{26}\text{Al}/^{10}\text{Be}$ ratio ( $\pm 1\sigma$ )
		$^{26}\text{Al}$	$^{10}\text{Be}$	$^{26}\text{Al}$	$^{10}\text{Be}$	$^{26}\text{Al}$		
AMC32	224.46 $\pm$ 5.61	1343.68 $\pm$ 40.9	65,701	57,257	9.19 $\pm$ 0.23	10.54 $\pm$ 0.32	5.99 $\pm$ 0.24	
AMC33	120.44 $\pm$ 3.76	763.95 $\pm$ 31.44	31,753	28,706	19.01 $\pm$ 0.59	21.03 $\pm$ 0.87	6.34 $\pm$ 0.33	
BAC34	81.13 $\pm$ 2.51	510.95 $\pm$ 18.5	26,497	23,997	22.79 $\pm$ 0.70	25.16 $\pm$ 0.91	6.30 $\pm$ 0.30	
BAC35	34.50 $\pm$ 1.08	231.73 $\pm$ 17.67	20,168	19,134	29.94 $\pm$ 0.94	31.56 $\pm$ 2.41	6.72 $\pm$ 0.55	
BAC36	26.35 $\pm$ 0.92	151.46 $\pm$ 28.47	15,250	12,306	39.59 $\pm$ 1.38	49.06 $\pm$ 9.22	5.75 $\pm$ 1.10	

<sup>a</sup> Calculation of denudation rates takes account of neutron- and muon-derived  $^{10}\text{Be}$  production, of correction coefficients for topography, soil and snow cover, and is based on Eq. (1). Bedrock density is 2.65 g/cm<sup>3</sup>.

(i.e., at the beginning of the Holocene: 11.7 ka). This implies that a bedrock layer <2–3 m was removed during the Würm and that a proportion of the TCN inventory measured in this sample is ascribable to preglacial exposure – most likely during the previous (Eemian) interglacial (see Section 5.2). The two samples from the Aneto cirque floor, AN09 and AN10, are situated immediately downvalley from the LIA moraine: these ice-polished bedrock steps lay consequently below ice during the Renclusa stade (Younger Dryas, GS-1). They yielded MEAs of  $14 \pm 0.4$  ka and  $13 \pm 0.4$  ka, respectively – both greater than the known age of ice retreat from these sites (~11.7 ka). Again, this implies that shallow bedrock denudation (<2–3 m) occurred during the Würm and that a proportion of the TCN concentration is probably inherited from exposure during the Eemian interglacial.

Finally, four samples collected from the two cirque floors inboard of the Holocene/LIA ice extent display exposure ages of  $4.8 \pm 0.2$  ka (MA11),  $6.1 \pm 0.2$  ka (MA12),  $7.1 \pm 0.25$  ka (AN13), and  $7.9 \pm 0.3$  ka (AN14). Given that the last deglaciation occurred at these sites between 1943 and 1973 (photographic evidence: René, 2011), the MEA range is much greater than the effective time of exposure of these bedrock surfaces. The entire nuclide inventory measured in those four samples accumulated over at least the duration of the early Holocene.

#### 4.1.2. Bassiès

In the Bassiès Range, two samples were collected at the Legunabens diffuence col. between the Escale and the Saleix valleys. The first is an erratic boulder (BA15:  $15.4 \pm 0.9$  ka) on the eastern side of the pass at 1673 m, and the second a polished bedrock step (BA16:  $15.8 \pm 0.8$  ka) located on the western side of the pass at 1739 m. These data are mutually consistent and show that cirque glaciers located on the north side of the Bassiès Range breached the Legunabens divide at the time of the Oldest Dryas (GS-2.1a). All the other samples from Bassiès were collected within the glaciated boundaries of the Mouscadous stade (Fig. 6B, Table 1). The two erratic boulders sampled on the Mouscadous lateral moraine (BA17:  $11.8 \pm 1.1$  ka and BA18:  $11.4 \pm 0.8$  ka) yielded a Younger Dryas (GS-1) age for this readvance, at which time the upper Escale valley contained a glacier 3 to 4 km long. The frontal moraine of this short valley glacier is unpreserved, but the longitudinal profile of the Mouscadous lateral moraine and the underlying bedrock topography suggest it stood ca. 1680–1700 m. On that basis, and based on the altitudes of the ridgetops above the Escale cirques (2600 m), the Younger Dryas ELA in the Bassiès Range coincided approximately with the 2150-m contour.

Several ice-polished bedrock surfaces occur inboard of the Mouscadous stadal moraine (Fig. 6B). Two of these yielded substantially younger MEAs than for the adjacent moraines: BA19 ( $8.7 \pm 0.5$  ka) and BA24 ( $8.7 \pm 0.3$  ka). These Holocene exposure ages can be explained by postglacial shielding of the sampled surfaces by glacial till. Another ice-polished surface yielded MEAs (BA20:  $12.3 \pm 0.7$  ka) compatible with a deglaciation of the sampled rock bar between the Younger Dryas and the early Holocene. Finally, the last three ice-polished surfaces yielded MEAs (BA21:  $15 \pm 0.5$  ka; BA22:  $15 \pm 0.5$  ka; BA23:  $13.4 \pm 0.5$  ka) somewhat older than suggested by the moraine-based deglaciation chronology. These MEAs indicate that the Würmian glacier removed bedrock thicknesses <2–3 m at these sites, where a

component of the TCN inventory inherited from the Eemian interglacial has thus been preserved.

#### 4.1.3. Carlit

Samples CAL29, CAL30, and CAL31 were collected inboard of the Oldest Dryas ice extent in the Llat cirque and yielded MEAs of  $26.5 \pm 4.4$  ka,  $26.2 \pm 3.9$  ka, and  $21.7 \pm 2.3$  ka, respectively (Fig. 7B). These values are much greater than the time elapsed since these bedrock steps were last deglaciated during the Bølling–Allerød (~14.7 ka). In the Cometa d'Espagne cirque, however, the continued presence of a cirque glacier during the Younger Dryas has been ascertained from TCN exposure ages on moraines immediately adjacent to the bedrock-step exposures (Delmas et al., 2008). Three of the MEAs on this cirque floor indicate ages compatible with deglaciation occurring during the earliest Holocene (CAC25:  $11 \pm 1.8$  ka; CAC26:  $12.1 \pm 1.5$ ; CAC27:  $12.1 \pm 2.7$  ka). Only one of the samples suggests large nuclide inheritance (CAC28:  $27.9 \pm 1.5$ ).

#### 4.2. Cirque-floor denudation rates: calculations using TCN inheritance

Analysis of the MEAs obtained for the ice-polished bedrock steps (see Section 5.1; Table 1) highlights that most samples display some potential for quantifying cirque-floor subglacial denudation rates from TCN inheritance. Because the glaciation chronology has been determined for each cirque of interest,  $t_{\text{postglacial}}$  and  $t_{\text{preglacial}}$  can be constrained in order to calculate the subglacial denudation rate. Table 2 compiles the data relevant to the successive ice advances that occurred during the Last Termination. In the case of ice-polished surfaces situated within the spatial boundaries of the Younger Dryas, the value of  $t_{\text{postglacial}}$  aggregates the Holocene (duration: 11.7 ka) and the Bølling–Allerød (duration: 1.8 ka), i.e., a total duration of 13.5 ka (palaeoenvironmental data for the region show that areas under ice during the Younger Dryas were in places deglaciated during the Bølling–Allerød; Reille and Andrieu, 1993; Millet et al., 2012; see Section 2.3). Adding these two periods of cirque-floor exposure allows the inheritance component ( $N_{\text{inherited}}$ ) acquired during the Eemian interglacial ( $t_{\text{preglacial}}$ : 15 ka; after van Kolschoten et al., 2003) to be calculated. From this, depths of subglacial bedrock denudation ( $z$ , in cm) during the Würm (100 ka) can be inferred. In the case of ice-polished rock surfaces situated within the spatial boundaries of the Oldest Dryas stade, exposure to cosmic rays has remained uninterrupted since the Bølling–Allerød interstade, in which case  $t_{\text{postglacial}}$  for MA03 is 14.7 ka. In the specific case of the Carlit, ice fluctuations in response to small changes in ELA were larger than in the steeper mountain ranges because of the extensive plateau topography present in the vicinity of the Pleistocene ELA (Fig. 7A; Delmas et al., 2008, 2009), so that the duration of postglacial exposure for samples such as CAL29, CAL30, and CAL 31 ( $t_{\text{postglacial}} = 17.2$  ka) is greater than in the other massifs (i.e., MA03). It includes the exposure time elapsed since the beginning of the Bølling–Allerød (i.e., 14.7 ka) and the 2.5 ka interval between the Global LGM and the beginning of the Oldest Dryas readvance. As in the previous cases,  $N_{\text{inherited}}$  is assumed to have accumulated during the Eemian interglacial ( $t_{\text{preglacial}} = 15$  ka), so that subglacial denudation depths ( $z$ , cm) during the Würm (100 ka) can be obtained as previously.

On that basis, seven ice-polished surfaces out of a total of fifteen samples situated within the boundaries of the Last Termination stadial readvances record components of inherited TCN, with corresponding Würmian subglacial denudation values ranging between 0 and 20–30 mm/ka (Table 2). Among the remaining eight samples, four other polished surfaces (MA07, AN09, BA23, and CAC 27) provide more borderline cases, for which it can nonetheless be estimated from their uncertainty intervals that maximum Würmian subglacial denudation was close to 3 m, yielding mean rates of ~30 mm/ka. In the case of the remaining four samples reported in Table 2, the  $^{10}\text{Be}$  clock was reset as a result of unspecifiable denudation depths exceeding 3 m. However, among those four samples, two are suitable for estimating subglacial denudation during the Younger Dryas glacial readvance (Table 3). Given that these ice-scoured surfaces were buried under ice during the Younger Dryas, nuclide accumulation began either at the beginning of the Holocene (assuming that the  $^{10}\text{Be}$  was entirely reset during the Younger Dryas) or at the beginning of the Bølling–Allerød (under the alternative assumption that the Younger Dryas glacial advance failed to reset the radiometric clock). These two hypotheses are tested in Table 3 by calculating values of  $z$  on the basis of  $t_{\text{postglacial}} = 11.7$  ka and  $t_{\text{preglacial}} = 1.8$  ka, while also assuming that the cirque glacier ice remained sufficiently thick to shield the underlying bedrock from the neutron flux and that muon-induced production at those subglacial depths remained negligible over those geologically brief time intervals. Results show that nuclide inheritance dating back to exposure during the Bølling–Allerød interstade is plausible in all cases and that subglacial denudation during the Younger Dryas ranged between 30 and 250–350 mm/ka.

Table 3 also includes the ice-polished surfaces situated within the boundaries of the LIA in the Maladeta range. The MEAs obtained from those four samples vary between 5 and 8 ka, but photographic evidence indicates that those rock surfaces have truly been exposed for only the last 50 years (René, 2011). This large discrepancy implies that the entire nuclide inventory was acquired during the early Holocene, i.e., before the last burial episode. The Holocene glacial chronology of the Pyrenees has not been widely studied (Gellatly et al., 1992; González Trueba et al., 2008; García-Ruiz et al., 2014). In the Alps, however, a wide array of geochronological data has been obtained for the Neoglacial from moraines (Ivy-Ochs et al., 2009), speleothems (Luetscher et al., 2011), and lacustrine deposits (Simonneau et al., 2013). All of these studies conclude that (i) climatic conditions during the earliest Holocene (11.6–10.5 ka) were similar to the Younger Dryas, with glaciers terminating either close to those of the Egesen (Younger Dryas) stadial moraines or farther upvalley but always outward of the LIA boundary. (ii) Between 10.5 and 3.3 ka, conditions in the Alps were not conducive to significant glacier expansion, except possibly during rare brief intervals (such as the 8.2 ka event) when small glaciers, less than a few  $\text{km}^2$ , may have advanced to positions close to their future LIA positions. (iii) The onset of mid-Holocene glacier recrudescence at some sites is indicated to have occurred as early as 5 ka, with glacier-friendly conditions after ~3.3 ka persisting until the end of the LIA. In detail, up to 13 century- to millennial-scale Neoglacial events have been detected in Europe (Matthews, 2013), yielding a signal of increasing magnitude and frequency that culminated in the late Holocene maximum (better known as the LIA). The absence of Holocene moraines outboard of the LIA glacial boundary suggests that the Maladeta range recorded Holocene glacier fluctuation magnitudes similar to, and synchronous with, those of the Alps and of other parts of Europe and the world (Solomina et al., 2015). On that basis, bedrock surfaces MA11, MA12, AN13, and AN14 recorded the following three-stage exposure history: (i) resetting of the  $^{10}\text{Be}$  clock during the Würm and uninterrupted burial until the earliest Holocene (11.7 ka; the assumption that those sites remained under ice during the Bølling–Allerød is inferred indirectly from the fact that they were later covered by glaciers during the LIA, and that the Holocene ELA rose 300 m above the Bølling–Allerød ELA); (ii) exposure during the early Holocene; followed by (iii) burial resulting from icefield

expansion after 3.3 ka by inference from the constraints held valid for the European Alps. The inferred value for  $t_{\text{preglacial}}$  is, therefore,  $11.7 - 3.3 = 8.4$  ka, with subglacial denudation spanning 3.3 ka (Table 3). During that time interval, subglacial denudation rates on the Maladeta and Aneto cirque floors were 5 to 110 mm/ka.

In summary, the Holocene cirque-floor denudation rates are comparable to those recorded during the Younger Dryas (i.e., tens to hundreds of mm/ka), but they are one order of magnitude greater than those recorded during the Würm (a few dozen mm/ka), i.e., at a time of icefield conditions when the cirques were feeding powerful outlet glaciers (Fig. 1).

#### 4.3. Steady-state denudation rates on supraglacial ridgetops

Some features observed on the ridgetops (a relatively thick weathering mantle of saprolite, extensive mats of lichen, absence of ice-polished and plucked surfaces) suggest these land surfaces were located above icefield trimlines during the successive glaciations of the Pleistocene. Absence of burial is confirmed by the  $^{26}\text{Al}/^{10}\text{Be}$  ratios ranging between 6 and 7 (Table 4), also suggesting a nuclide steady state under an uninterrupted denudation regime. These summits were consequently continuously exposed as nunataks. Table 4 also shows that MEAs measured on the supraglacial ridgetops are always greater than those provided by the cirque floors (Table 1). In this supraglacial environment continually exposed to nonglacial denudation, the evidence suggests comparatively lower denudation rates than on the cirque floors. The differences between the bedrock and the regolith ridgetops are ascribable to differences in sampled rock materials (i.e., bedrock vs. saprolite) and their respective susceptibilities to a range of surface processes rather than to the intrinsic contrasts in ridgetop morphologies (i.e., arête vs. paleic).

On the arête-shaped supraglacial bedrock ridgetops, the mean denudation rates are low (10–20 mm/ka) and scale with relatively long integration times (~30–60 ka). The range in integration times indicates variable intensities through space and time and suggests that those bedrock headwalls evolved under the effect of periodic mass movement. In response to small fluctuations in ice thickness in the cirque zone during icefield conditions or to more severe deglacial rockwall debuttressing events, rockfall events were capable of removing rock masses sufficiently large to partially reset the  $^{10}\text{Be}$  clock on the freshly exposed rockfall scars. Between such events the ridgetops accumulated nuclides under a low-energy regime defined by the AMC 32 and AMC33 mean denudation rates. The flat paleic bedrock ridgetop above the Escale cirque (BAC34; Figs. 4C, 6) in the Bassiès Range attained a somewhat greater denudation rate ( $22.8 \pm 0.7$  mm/ka), consistent with the fact that the saprolite has been stripped down to the weathering front.

Values on the flat, regolith-bearing paleic ridgetops in Bassiès (BAC35:  $29.9 \pm 0.9$  mm/ka and BAC36:  $39.6 \pm 1.4$  mm/ka) are higher and accordingly valid over much shorter integration times. They provide averages of denudation over the last 21 to 15 ka and measure the stripping rates that occurred subsequent to thawing of the permafrost during deglaciation (i.e., probably during half the estimated integration time) but before the land surface became stabilized by vegetation and a thick humus horizon in the early Holocene (Fig. 4C). Clearly, the TCN denudation rates on ridgetops capture very specific processes operating within a limited time window defined by the integration time and cannot be readily extrapolated to the Pleistocene or balanced against longer-term crustal uplift. Based on the depth of exposed weathering fronts on other elevated paleic surfaces in the Ariège catchment (Calvet and Gunnell, 2008; Calvet et al., 2015b), initial stocks of grus were likely 50 m thick or more. Sustained stripping of grus and corestones at rates of 3 to 5 cm/ka throughout the Quaternary would be incompatible with the preservation of these currently extant masses of weathered granite, even when assuming that weathering fronts can deepen to some extent during 15 to 20 ka-long interglacials at elevations of 2 km or more. Stripping of regolith on the paleic surfaces was

therefore rapid but discontinuous, most of the time preserved by permafrost but thinned during relatively short deglacial intervals.

## 5. Discussion

### 5.1. Cirque-floor subglacial denudation rates: first results obtained for an entire glacial/deglacial cycle

Barr and Spagnolo (2015) pointed out the very small ( $n = 12$ ) number of denudation-rate studies dealing with alpine cirques. Furthermore, most of the existing data deal with short time intervals (a few ka) because they are based on the estimated volumes of sediments produced by cirque glaciers during the Last Termination or the Holocene. A few studies have produced results covering longer timescales (a few  $10^5$  ka) by quantifying changes in the size of cirque volume during the Pleistocene (Andrews and LeMasurier, 1973; Olyphant, 1981; Brook et al., 2006). Apart from the sediment budget calculated for an active cirque-glacier environment in British Columbia (Sanders et al., 2013), all the data currently available constrain bulk denudation in the cirque zone and do not distinguish between the respective contributions from the cirque floor, the head- and sidewalls, and the ridgetops. Cirque-relevant data valid for an entire glacial cycle are likewise scarce, usually because the research focuses on entire icefields (e.g., Elverhøi et al., 1995; Glasser and Hall, 1997; Buoncristiani and Campy, 2001) or on land units situated at lower elevations (e.g., glacial troughs and adjacent interfluvies: Fabel et al., 2002, 2004; Stroeven et al., 2002; Marquette et al., 2004; Li et al., 2005; Staiger et al., 2005; Briner et al., 2006, 2008) rather than on the cirque zone itself.

This study provides a first estimation of subglacial denudation in a population of alpine cirque floors over the course of an entire glacial/deglacial cycle. The setting provides scope for detecting differences in denudation intensity in two contrasting situations: maximum icefield conditions (Table 2), at a time when the cirque zone was situated in an elevation belt much above the regional ELA, and deglacial to interglacial conditions (Table 3), at a time when the regional ELA roughly coincided with cirque-floor altitudes and the icefield was reduced to a population of individual cirque glaciers. Additional opportunities are afforded for quantifying Younger Dryas and Holocene denudation separately. The value of capturing mean subglacial cirque denudation rates over an entire glacial cycle is the potential for extrapolating these to at least the entire late Pleistocene and allows the contribution of cirque glaciers to the overall topographic evolution of Pyrenean mountain ranges to be appreciated. Finally, the data provide an opportunity for testing the glacial buzzsaw hypothesis on the merits of a measurement protocol never previously implemented for that purpose. The buzzsaw is usually inferred from range-scale morphometric signatures or from thermochronological data typically relevant to Cenozoic-scale base-level changes, whereas here the TCN integration times and denudation rates focus on direct dating of glacial landforms.

### 5.2. Constraints on subglacial denudation rates

The three ideal scenarios guiding the method for extracting subglacial denudation rates from TCN exposure ages were presented in Section 3.1.1. Given the parameters entered in Eq. (1), these simple scenarios could theoretically suffer plausible complications. The two major twists, neither of which are exclusive to one another, are described here. (i) Preglacial nuclide concentrations were calculated while assuming no denudation during the time of preglacial nuclide accumulation (i.e., during the Eemian interglacial; Fig. 8). While such a hypothesis remains valid for the Holocene interglacial because all the surfaces sampled on the cirque floors display well-preserved ice-scour features, this hard evidence becomes less certain for preglacial conditions. Therefore, in a case where nuclide accumulation occurred during preglacial times under an erosive regime, then concentrations reported in Tables 2 and 3—including the associated  $z$  values and subglacial denudation

rates—should be interpreted as overestimates. (ii) The second theoretical complication will arise when exposure of the sampled bedrock surfaces gets delayed by till cover persisting for some time after the last subglacial burial event. In this case, the inferred nuclide inheritance values will be greater than those estimated in the results tables, with resulting subglacial denudation values accordingly expected to be lower. Independent evidence in support of either of the two theoretical scenarios just described is entirely lacking from the field sites and can only be a matter of speculation. However, the geomorphological uncertainty bedevilling those scenarios is redeemed by the fact that both types of error play in favour of making subglacial denudation even less efficient than suggested in Tables 2 and 3, where all reported rates are consequently confirmed to be maximum rates.

As also previously emphasized in Section 3.3.1, another key point is that the method can only provide precise measurements at sites where resetting of the  $^{10}\text{Be}$  clock did not occur, i.e., where bedrock stripping did not exceed 3 to 4 m. In this study, such was the case for 12 out of a total of 19 samples. In the case of sites affected by a full reset ( $n = 2$ : MA03 and CAC26), establishing by how much the 3–4 m denudation envelope was exceeded is impossible. In borderline cases where the uncertainty interval around  $N_{\text{measured}}$  overlaps with the resetting domain ( $n = 5$ ),  $z$  is unspecifiable. Lastly, the results presented in Tables 2 and 3 are minimum values in the sense that the cirque-floor sampling sites systematically targeted were protruding roches moutonnées rather than dips or grooves in the bedrock (where channelled and/or thicker ice is potentially more erosive). Nevertheless, the low bedrock relief of the sloping cirque-floor surfaces (measured as 5–10 m in the Aneto from a 5-m ground resolution digital elevation model) suggests that spatial variation in denudation depths across individual cirque floors was limited. To summarize, the method in this study provides an upper and lower bracket of maximum denudation rates (Tables 2 and 3) for bedrock exposure sites where subglacial denudation on cirque floors has been minimal.

### 5.3. Pyrenean cirque denudation values: global comparison with results from other settings

Reported results reveal some scatter, but a clear, order-of-magnitude contrast distinguishes the denudation rates inferred for the entire Würm (Table 2) from the deglacial and interglacial rates of the Younger Dryas and Holocene (Table 3). For the Würm, the largest values attain a few dozen mm/ka, with only two fully reset samples (MA03 and AN10). These rates scale with some of the lowest values reported in the literature on glacial denudation (Hallet et al., 1996; Delmas et al., 2009; Koppes and Montgomery, 2009), irrespective of the timescale or estimation method considered. One similar case was the Carlit Range, where it was estimated that the Würmian icefield removed an average bedrock thickness of ~5 m across the landscape (Delmas et al., 2009). In the case of the Younger Dryas and Holocene, the range of values rises from tens to hundreds of mm/ka, thereby converging with rates obtained independently from moraine volumes produced by cirque glaciers over similar time spans (a few ka). Bottom bracket values of 8 to 76 mm/ka are reported from Baffin Island (a shield environment; Anderson, 1978), and top bracket rates of 5000 to 6000 mm/ka have been obtained in the Cascades (Hicks et al., 1990) and Southern Alps of New Zealand (Mills, 1979) — two of the most humid and rapidly rising mountain ranges in the world. The largest population of reported values falls between 100 and 900 mm/ka (Reheis, 1975; Larsen and Mangerud, 1981; Bogen, 1996; Sanders et al., 2013). In the eastern Pyrenees, the total volume of moraine produced by cirque glaciers still active during the Last Termination in the SE Carlit converted to a glacial denudation rate of 180 to 340 mm/ka depending on the chosen sediment to bedrock density ratio (Delmas et al., 2009). In summary, denudation estimates based on TCN MEAs would seem to produce minimum values of similar magnitude to those obtained from other methods over a similar time window.

#### 5.4. Variation in denudation rates over time: Würmian exceeded by Holocene

A clear rise in cirque denudation rates is detectable during the deglacial and interglacial periods of lighter cirque glaciation compared to the full icefield conditions of the Würm. Würmian denudation rates obtained from CAL29 (0.3–6.2 mm/ka), CAL 30 (0.7–6.3 mm/ka), and CAL 31 (4–12.9 mm/ka) are considerably lower than the average rate inferred for the entire icefield (50 mm/ka, [Delmas et al., 2009](#)), indicating that cirque floors in the Carlit were not major sources of glacial debris during extended icefield conditions. The relative infirmity of glacial denudation in the cirque zone during full glacial conditions likely arose from the correspondingly depressed ELA, which descended to elevations much below the cirque floors and, therefore, focused maximum subglacial denudation lower into the valleys ([Cook and Swift, 2012](#); [Barr and Spagnolo, 2015](#)). During these icefield conditions, the cirques contained relatively thin ice given the low headwall relief and flat, sloping floor that define the typical *van* morphology. The velocity of these glaciers was low because of the limited ice thickness and low ice gradient between the iceshed and the thick outlet glaciers filling the glacial troughs – in sharp contrast with environmental conditions more typical of the subsequent deglacial to interglacial conditions, during which the focus of subglacial denudation rises progressively from the troughs to the cirques as the icefield contracts ([Cook and Swift, 2012](#)). Low denudation rates in glacial environments can be attributed to the occurrence of cold-based glaciers or to a glacier surface gradient  $< 7^\circ$ , deemed insufficiently steep to promote rotational ice flow (and hence to producing deep, *armchair* cirques; [Evans, 1999](#)). Here, the cold-based glacier hypothesis is plausible at least for the colder periods of the Würm. The thin glaciers at high elevations ( $> 2500$ – $3000$  m) would have established themselves on frozen ground and would not have offered much protection from the very low atmospheric temperatures. The low-gradient glacier hypothesis may have been effective in the context of the Escal cirque ([Fig. 3](#)) and on the Carlit paleic pediment ([Fig. 4](#)) but does not appear particularly relevant to other cirques of the Maladeta range or to the Cometa d'Espagne (Carlit) cirques, where cirque-floor slope angles exceed  $25^\circ$  and higher-relief headwalls were capable of accommodating thicker Würmian glaciers. In the latter case, glacier infirmity during extended icefield conditions is ascribable to an interruption of debris supply to the glacier system from headwall and ridgetop surfaces (glacier load starvation hypothesis). In contrast, during warmer (temperate) times when glaciers were restricted to the cirque zone, daily and seasonal variations in temperature would favour frost cracking and ridgetop weakening, thus indirectly enhancing subglacial denudation in the cirque zone by providing debris to the sliding glacier base. A similar mechanism was described by [Scherler \(2015\)](#) in the Khumbu Himalaya (eastern Nepal), where frost cracking promoted higher denudation rates at sites where cirque glaciers were able to evacuate the debris and maintain ice-free bedrock headwalls, thus preventing the accumulation of scree deposits. Finally, glacial denudation on cirque floors in the Pyrenees intensified during the colder spikes of the Last Termination (e.g., the Younger Dryas), probably because the cirque glaciers (i) were steeper than during full interglacials (consequently favouring rotational slip and higher rates of basal sliding) and (ii) met with periglacial and paraglacial conditions promoting greater debris input to the glacial system (reduced load starvation) than during extended icefield periods.

#### 5.5. Spatial variations in denudation across the alpine cirque zone

Spatial variation across the three study areas is difficult to characterize given the finite number of sampling sites. Unsurprisingly, MA08 is situated on a transfluence col and provides the lowest rates of the data set. The sites that underwent total or partial resetting are relatively randomly distributed in terms of ice stream trajectories. Results from all the other sites exhibit tenuous correlations with the mesoscale bedrock

topography, none worthy of discussion. Of greater interest is the difference in denudation rate between the ridgetops and the cirque floors. The steady-state denudation values for arête samples AMC32, AMC33, and BAC34 ([Table 4](#)) range between 10 and 25 mm/ka. Sample AMC32 displays the longest integration time (scaling with the entire Würm), but overall the Würmian ridgetop maximum denudation rates are similar to or lower than their cirque-floor counterparts (a few dozen mm/ka). Cirque deepening, i.e., divergent denudation between cirque floors and ridgetops, operated more efficiently during temperate periods. In the eastern and central Pyrenees, however, the total mass balance remained quite small given that total denudation obtained for the Younger Dryas and Holocene combined was 0.3 to 3 m. By extrapolation, these values imply 3 to 30 m in similar deglacial and interglacial conditions over the last 10 major Pleistocene deglacial/interglacial cycles.

#### 5.6. Cirque glaciers: more powerful during interglacials than during glacials

Mean mountain uplift rates over the last 10 Ma for the central (60–190 mm/ka; [Ortuño et al., 2013](#)) and eastern Pyrenees ( $> 80$  mm/ka; [Calvet and Gunnell, 2008](#); [Gunnell et al., 2008, 2009](#)) have been inferred on the basis of indirect methods such as LTT, palaeobotanical altimetry, micromammalian biochronology, and geomorphological indices. The continuation of crustal uplift into the Quaternary has been inferred from canyon incision rates (50–100 m/Ma; [Calvet et al., 2015a](#)). Evidence of tectonic motions in more recent times, however, is inconclusive because existing GPS-derived data are reported to be unworkable for inferring vertical displacements ([Rigo et al., 2015](#)). Compared nonetheless to the various Cenozoic uplift rates given above, the Würmian glacial denudation values obtained for the majority of cirque floors and ridgetops were clearly much lower – except during the brief interglacial periods when cirque denudation rates attained similar magnitudes at some sites. On that basis, some growth in relief and elevation is likely to have occurred intermittently within the cirque zone during the Quaternary. During glacial stages, the maximum denudational response to uplift would have occurred instead below the Pleistocene ELA, i.e., the glacial troughs, with the ensuing growth in relief affecting a broader elevation band than during interglacial conditions.

In total, the results of this study do not support the glacial buzzsaw as a relevant Quaternary landscape evolution model for the eastern and central Pyrenees: apart from a few tenuous hints, there is no evidence that the Pyrenean icefield was sufficiently powerful to sustain a long-term balance with the mean crustal uplift rate. The times when a glacier-driven local balance might have occurred were brief and coincided with deglacial and interglacial cirque glaciation rather than with icefield conditions. Furthermore, topographic lowering did not impact supraglacial ridgetops in a major way (ridgetop denudation rates remained low, including at transfluence cols; e.g., MA08: 1.8–2.6 mm/ka). Many cirque-floor surfaces underwent glacial denudation at rates exceeding 30 mm/ka – clearly higher than rates recorded on ridgetops (10–25 mm/ka). The only detectable trend in the glaciated ranges of the central and eastern Pyrenees, therefore, is one of gradually increasing local relief occurring alternately in the cirque zone (during interglacials) and in the valleys (during glacials). Such evidence of growth in local relief does not support the buzzsaw hypothesis, according to which ridgetops and cirque floors are expected instead to erode at the same rate.

## 6. Conclusion

The cirque-floor denudation rates calculated using TCN inheritance provide rates of 0–120 mm/ka, with some values  $> 300$  mm/ka, that scale with some of the lowest values encountered in the literature on glacial denudation irrespective of the timescale or estimation method considered. The results highlight that subglacial denudation in the alpine cirques of the eastern and central Pyrenees was greater during

waning glacial periods and glacial resurgences during deglacial and interglacial periods, i.e., when the icefield was reduced to a population of cirque glaciers, than during extended icefield conditions. During glacial periods, relative glacier infirmity in the cirque zone may have resulted from three nonexclusive conditions: cold-based glaciers; shallow, low-gradient glaciers (absence of rotational flow); and glacier-load starvation (because permafrost drastically decreases the potential for clast supply from nunataks to the glaciers). During the colder oscillations of the Last Termination (e.g., Younger Dryas) and of the Holocene, conditions switched in favour of accelerated cirque denudation: cirque glaciers became steeper, warmer-based, and atmospheric mean temperatures warmer than during the Würm promoted frost cracking and supraglacial ridgetop weakening, thus indirectly enhancing subglacial denudation in the cirque zone by providing debris to the sliding glacier base (Scherler, 2015). This finding is consistent with regional evidence from South America (Koppes et al., 2015), where glaciers have been found to erode 100 to 1000 times faster in contexts of rising temperatures. This finding also has implications for extrapolating to former Pleistocene glacial environments denudation rates that were measured in modern (interglacial) cirque environments under the assumption (in this case spurious) that discrete cirque glaciers in temperate conditions are less efficient sediment delivery systems than when they form components of a more powerful regional icefield.

Whatever the Quaternary rock uplift rates of the Axial Zone, which are poorly known, the contrast between ridgetop lowering rates and cirque deepening rates during the Würm suggests that cirques have tended to deepen, thus increasing local relief in the cirque zone. Glacial processes were thus not sufficient to bring the topography to a buzzsaw equilibrium. The results thus also urge caution against drawing conclusions about the glacial buzzsaw exclusively from static criteria such as morphometric variables and hypsometric proxies, which can provide spurious indications (for a discussion on the Alps, see Robl et al., 2015b). For example, some ranges in this study display diagnostic features compatible with glacial denudation and with hints to perhaps a low-energy glacial buzzsaw in the Maladeta, such as accordant ridgetops and a hypsometric maximum occurring between the Pleistocene ELA and the modern ELA. Some of those features, however — particularly in the Carlit and Bassiès ranges — are vestiges of paleic surfaces and pediments of Cenozoic age rather than features of an alpine Gipfelflur (Calvet et al., 2015b). The hypsometry of the study area (Fig. 2) also deviates from certain other features held to be diagnostic of the buzzsaw, such as relief above the Pleistocene ELA, which is ~1000 m in the Maladeta and Bassiès and thereby exceeds the values measured by Mitchell and Humphries (2014) on a global scale (mean local relief:  $346 \pm 107$  m, rarely exceeding 600 m). The buzzsaw hypothesis is also at odds with the increase in  $^{10}\text{Be}$  MEAs as a function of elevation, with old MEAs (26–28 ka) on cirque floors in the Carlit and at the transfluence col between the Aneto and Maladeta cirques (MA08: 24 ka), and MEAs older still on the bedrock ridgetops (66 and 33 ka on the arête between the Aneto and Maladeta cirques). According to the buzzsaw principle, rapid cirque headwall recession since the onset of the Würmian glaciation should have resulted in rapid ridge intersection and lowering. The long integration times and the presence of weathered bedrock on these arêtes suggest instead that cirque evolution in the study area did not proceed at very high rates in this way.

In conclusion, the inference of growing relief permitted by the measurable TCN denudation imbalance between supraglacial ridgetops and cirque floors diverges from the basic assumption of the glacial buzzsaw, which states that the erosive power of small and large glaciers can keep pace with rock uplift rates and have a limiting effect on ridgetop heights. The typical *van* shape of the cirques studied in the Maladeta and Bassiès, with outward-sloping floors exceeding slope angles of 20° and low-relief head- and sidewalls situated high above the Pleistocene ELA, deviates markedly from the expectations postulated by the buzzsaw hypothesis — perhaps even suggesting that *van* cirques, reminiscent of the *flat* cirques reported by Mindrescu and Evans (2014) in Romania,

are potentially good proxy indicators of mountain range evolution that violates the buzzsaw principle.

Supplementary data to this article can be found online at doi:10.1016/j.geomorph.2016.10.035.

## Acknowledgements

This research was funded by a research grant from the University of Perpignan–Via Domitia. We thank the four anonymous reviewers for their insightful comments on the manuscript.

## References

- Anders, A.M., Mitchell, S.G., Tomkin, J.H., 2010. Cirques, peaks, and precipitation patterns in the Swiss Alps: connections among climate, glacial erosion, and topography. *Geology* 38, 239–242.
- Anderson, L.W., 1978. Cirque glacier erosion rates and characteristics of Neoglacial tills, Pangnirtung Fjord area, Baffin Island, NWT, Canada. *Arct. Alp. Res.* 10, 749–760.
- Andrews, J.T., LeMasurier, W.E., 1973. Rates of Quaternary glacial erosion and corrie formation, Marie Byrd Land, Antarctica. *Geology* 1, 75–80.
- Arnold, M., Merchel, S., Bourlès, D.L., Braucher, R., Benedetti, L., Finkel, R.C., Aumaître, G., Gottsdang, A., Klein, M., 2010. The French accelerator mass spectrometry facility ASTER: improved performance and developments. *Nuclear Instrumentation Methods in Physics Research, Section B: Beam Interactions with Materials and Atoms*. 268, pp. 1954–1959.
- Barr, I.D., Spagnolo, M., 2015. Glacial cirques as palaeoenvironmental indicators: their potential and limitations. *Earth Sci. Rev.* 151, 48–78.
- Berger, A.L., Gulick, S.P.S., Spotila, J.A., Upton, P., Jaeger, J.M., Chapman, J.B., Worthington, L.A., Pavlis, T.L., Ridgway, K.D., Willems, B.A., McAleer, R.J., 2008. Quaternary tectonic response to intensified glacial erosion in an orogenic wedge. *Nat. Geosci.* 1, 793–799.
- Bogen, J., 1996. Erosion rates and sediment yields of glaciers. *Ann. Glaciol.* 22, 48–52.
- Braucher, R., Merchel, S., Borgomano, J., Bourlès, D.L., 2011. Production of cosmogenic radionuclides at great depth: a multi element approach. *Earth Planet. Sci. Lett.* 309, 1–9.
- Briner, J.P., Kaufman, D.S., Manley, W.F., Finkel, R.C., Caffee, M.W., 2005a. Cosmogenic exposure dating of late Pleistocene moraine stabilization in Alaska. *Geol. Soc. Am. Bull.* 117, 1108–1120.
- Briner, J.P., Miller, G.H., Davis, P.T., Finkel, R.C., 2005b. Cosmogenic exposure dating in Arctic glacial landscapes: implications for the glacial history of northeastern Baffin Island, Arctic Canada. *Can. J. Earth Sci.* 42, 67–84.
- Briner, J.P., Miller, G.H., Davis, P.T., Finkel, R., 2006. Cosmogenic radionuclides from fjord landscapes support differential erosion by overriding ice sheets. *Geol. Soc. Am. Bull.* 118, 406–420.
- Briner, J.P., Miller, G.H., Finkel, R., Hess, D.P., 2008. Glacial erosion at the fjord onset zone and implications for the organization of ice flow on Baffin Island, Arctic Canada. *Geomorphology* 97, 126–134.
- Brocklehurst, S.H., Whipple, K.X., 2002. Glacial erosion and relief production in the Eastern Sierra Nevada, California. *Geomorphology* 42, 1–24.
- Brocklehurst, S.H., Whipple, K.X., 2004. Hypsometry of glaciated landscapes. *Earth Surf. Process. Landf.* 29, 907–926.
- Brook, M.S., Kirkbride, M.P., Brock, B.W., 2006. Cirque development in a steadily uplifting range: rates of erosion and long-term morphometric change in alpine cirques in the Ben Ohau range, New Zealand. *Earth Surf. Process. Landf.* 31, 1167–1175.
- Brown, E.T., Edmond, J.M., Raisbeck, G.M., Yiou, F., Kurz, M.D., Brook, E.J., 1991. Examination of surface exposure ages of Antarctic moraines using in situ produced  $^{10}\text{Be}$  and  $^{26}\text{Al}$ . *Geochim. Cosmochim. Acta* 55, 2269–2283.
- Brozović, N., Burbank, D.W., Meigs, A.J., 1997. Climatic limits on landscape development in the northwestern Himalaya. *Science* 276, 571–574.
- Buoncrisiani, J.F., Campy, M., 2001. Late pleistocene detrital sediment yield of the Jura Glacier, France. *Quat. Res.* 56, 51–61.
- Calvet, M., 1996. Morphogenèse d'une montagne méditerranéenne: les Pyrénées orientales. Documents du BRGM, Orléans, v. 255, (1177 p).
- Calvet, M., Gunnell, Y., 2008. Planar landforms as markers of denudation chronology: an inversion of East Pyrenean tectonics based on landscape and sedimentary basin analysis. *Geol. Soc. Lond. Spec. Publ.* 296, 147–166.
- Calvet, M., Delmas, M., Gunnell, Y., Braucher, R., Bourlès, D., 2011. Recent advances in research on Quaternary glaciations in the Pyrenees. *Dev. Quat. Sci.* 15, 127–139.
- Calvet, M., Gunnell, Y., Braucher, R., Hez, G., Bourlès, D., Guillou, V., Delmas, M., 2015a. Groundwater karst as a proxy for measuring post-orogenic uplift: evidence from cosmogenic dating of alluvium-filled caves in the Pyrenees. *Geomorphology* 246, 617–633.
- Calvet, M., Gunnell, Y., Farines, B., 2015b. Flat-topped mountain ranges: their global distribution and value for understanding the evolution of mountain topography. *Geomorphology* 241, 255–291.
- Champagnac, J.D., Molnar, P., Sue, C., Herman, F., 2012. Tectonics, climate, and mountain topography. *J. Geophys. Res. Solid Earth* 117, B02403. <http://dx.doi.org/10.1029/2011JB008348>.
- Champagnac, J.D., Valla, P.J., Herman, F., 2014. Late-Cenozoic relief evolution under evolving climate: a review. *Tectonophysics* 614, 44–65.
- Chmieleff, J., von Blanckenburg, F., Kossert, K., Jakob, D., 2010. Determination of the  $^{10}\text{Be}$  half-life by multicollector ICP-MS and liquid scintillation counting. *Nuclear Instrumentation Methods in Physics Research, Section B: Beam Interactions with Materials and Atoms*. 268, pp. 192–199.

- Chueca Cía, J., Julián Andrés, A., Saz Sánchez, M.A., Creus Novau, J., López Moreno, J.I., 2005. Responses to climatic changes since the Little Ice Age on the Maladeta Glacier (Central Pyrenees). *Geomorphology* 68, 167–182.
- Cook, S.J., Swift, D.A., 2012. Subglacial basins: their origin and importance in glacial systems and landscapes. *Earth Sci. Rev.* 115, 332–372.
- Copons, R., Bordonau, J., 1997. El último ciclo glacial (Pleistoceno Superior-Holoceno) en el macizo de la Maladeta (Pirineos Centrales). *Rev. Soc. Geol. Esp.* 10, 55–66.
- Delmas, M., 2005. La déglaciation dans le massif du Carlit (Pyrénées orientales): approches géomorphologique et géochronologique nouvelles. *Bulletin de l'Association Française pour l'Etude du Quaternaire*. 16, pp. 45–55.
- Delmas, M., Gunnell, Y., Braucher, R., Calvet, M., Bourlès, D., 2008. Exposure age chronology of the last glaciation in the eastern Pyrenees. *Quat. Res.* 69, 231–241.
- Delmas, M., Calvet, M., Gunnell, Y., 2009. Variability of erosion rates in the Eastern Pyrenees during the last glacial cycle—a global perspective with special reference to the Eastern Pyrenees. *Quat. Sci. Rev.* 28, 484–498.
- Delmas, M., Calvet, M., Gunnell, Y., Braucher, R., Bourlès, D., 2011. Palaeogeography and  $^{10}\text{Be}$  exposure-age chronology of Middle and Late Pleistocene glacier systems in the northern Pyrenees: implications for reconstructing regional palaeoclimates. *Palaeogeogr. Palaeoclimatol. Palaeoecol.* 305, 109–122.
- Delmas, M., Calvet, M., Gunnell, Y., Braucher, R., Bourlès, D., 2012. Les glaciations quaternaires dans les Pyrénées ariégeoises: approche historiographique, données paléogéographiques et chronologiques nouvelles. *Quaternaire* 23, 61–85.
- Delmas, M., Gunnell, Y., Calvet, M., 2014. Environmental controls on alpine cirque size. *Geomorphology* 206, 318–329.
- Delmas, M., Gunnell, Y., Calvet, M., 2015. A critical appraisal of allometric growth among alpine cirques based on multivariate statistics and spatial analysis. *Geomorphology* 228, 637–652.
- Densmore, M.S., Ehlers, T.A., Woodsworth, G., 2007. Effect of Alpine glaciation on thermochronometer age-elevation profiles. *Geophys. Res. Lett.* 34, L02502. <http://dx.doi.org/10.1029/2006GL028371>.
- Denton, G.H., Anderson, R.F., Toggweiler, J.R., Edwards, R.L., Schaefer, J.M., Putnam, A.E., 2010. The last glacial termination. *Science* 328, 1652–1656.
- Dunai, T.J., 2010. *Cosmogenic Nuclides: Principles, Concepts and Applications in the Earth Surface Sciences*. Cambridge University Press (198 p).
- Dunne, J., Elmore, D., Muzikar, P., 1999. Scaling factors for the rates of production of cosmogenic nuclides for geometric shielding and attenuation at depth on sloped surfaces. *Geomorphology* 27, 3–11.
- Egholm, D.L., Nielsen, S.B., Pedersen, V.K., Lesemann, J.-E., 2009. Glacial effects limiting mountain height. *Nature* 460, 884–887.
- Ehlers, T.A., Farley, K.A., Rumsore, M.E., Woodsworth, G.J., 2006. Apatite (U–Th)/He signal of large-magnitude accelerated glacial erosion, southwest British Columbia. *Geology* 34, 765–768.
- Elverhøi, A., Svendsen, J.I., Solheim, A., Andersen, E.S., Milliman, J., Mangerud, J., Hooke, R.L., 1995. Late Quaternary sediment yield from the high arctic Svalbard area. *J. Geol.* 103, 1–17.
- Evans, I.S., 1999. Was the cirque glaciation of Wales time-transgressive, or not? *Ann. Glaciol.* 28, 33–39.
- Evans, I.S., Hall, A.M., Kleman, J., 2015. Glacial cirques and the relationship between equilibrium line altitudes and range height. *Geology*, e366 <http://dx.doi.org/10.1130/G36667C.1>.
- Fabel, D., Stroeven, A.P., Harbor, J., Kleman, J., Elmore, D., Fink, D., 2002. Landscape preservation under Fennoscandian ice sheets determined from in situ produced  $^{10}\text{Be}$  and  $^{26}\text{Al}$ . *Earth Planet. Sci. Lett.* 201, 397–406.
- Fabel, D., Harbor, J., Dahms, D., James, A., Elmore, D., Horn, L., Daley, K., Steele, C., 2004. Spatial patterns of glacial erosion at a valley scale derived from terrestrial cosmogenic  $^{10}\text{Be}$  and  $^{26}\text{Al}$  concentrations in rock. *Ann. Assoc. Am. Geogr.* 94, 241–255.
- Fernandez, R.A., Anderson, J.B., Wellner, J.S., Hallet, B., 2011. Timescale dependence of glacial erosion rates: a case study of Marinelli Glacier, Cordillera Darwin, southern Patagonia. *J. Geophys. Res.* Earth 116, F01020. <http://dx.doi.org/10.1029/2010JF001685>.
- Fillon, C., van der Beek, P., 2012. Post-orogenic evolution of the southern Pyrenees: constraints from inverse thermo-kinematic modelling of low-temperature thermochronology data. *Basin Res.* 24, 418–436.
- Foster, D., Brocklehurst, S.H., Gawthorpe, R.L., 2008. Small valley glaciers and the effectiveness of the glacial buzzsaw in the northern Basin and Range, USA. *Geomorphology* 102, 624–639.
- García-Ruiz, J.M., Bordonau, J., Martínez de Pisón, E., Vilaplana, J.M., 1992. Mapa geomorfológico de Benasque, 1:50,000 scale, M.T.N. 180. Geoforma Ediciones, Logroño, p. 4.
- García-Ruiz, J.M., Gómez-Villar, A., Ortigosa, L., Martí-Bono, C., 2000. Morphometry of glacial cirques in the Central Spanish Pyrenees. *Geogr. Ann. Ser. B* 82, 433–442.
- García-Ruiz, J.M., Palacios, D., de Andrés, N., Valero-Garcés, B.L., López-Moreno, J.I., Sanjuán, Y., 2014. Holocene and “Little Ice Age” glacial activity in the Marboré Cirque, Monte Perdido Massif, Central Spanish Pyrenees. *The Holocene* 24, 1439–1452.
- Gellatly, A.F., Grove, J.M., Switzer, V.R., 1992. Mid-Holocene glacial activity in the Pyrenees. *The Holocene* 2, 266–270.
- Gibson, M., Sinclair, H.D., Lynn, G.J., Stuart, F.M., 2007. Late to postorogenic exhumation of the Central Pyrenees revealed through combined thermochronological data and modelling. *Basin Res.* 19, 323–334.
- Gjermundsen, E.F., Briner, J.P., Akçar, N., Foros, J., Kubik, P.W., Salvigsen, O., Hormes, A., 2015. Minimal erosion of Arctic alpine topography during late Quaternary glaciation. *Nat. Geosci.* 8, 789–792.
- Glasser, N.F., Hall, A.M., 1997. Calculating quaternary glacial erosion rates in northeast Scotland. *Geomorphology* 20, 29–48.
- González Trueba, J.J., Martín Moreno, R., Martínez de Pisón, E., Serrano, E., 2008. Little Ice Age glaciation and current glaciers in the Iberian Peninsula. *The Holocene* 18, 551–568.
- Goodfellow, B., 2007. Relict non-glacial surfaces in formerly glaciated landscapes. *Earth Sci. Rev.* 80, 47–73.
- Gosse, J.C., Phillips, F.M., 2001. Terrestrial in situ cosmogenic nuclides: theory and application. *Quat. Sci. Rev.* 20, 1475–1560.
- Gunnell, Y., Zeyen, H., Calvet, M., 2008. Geophysical evidence of a missing lithospheric root beneath the Eastern Pyrenees: consequences for post-orogenic uplift and associated geomorphic signatures. *Earth Planet. Sci. Lett.* 276, 302–313.
- Gunnell, Y., Calvet, M., Bricchau, S., Carter, A., Aguilar, J.-P., Zeyen, H., 2009. Low long-term erosion rates in high-energy mountain belts: insights from thermo- and biochronology in the Eastern Pyrenees. *Earth Planet. Sci. Lett.* 278, 208–218.
- Gunnell, Y., Jarman, D., Braucher, R., Calvet, M., Delmas, M., Léanni, L., Bourlès, D., Arnold, M., Aumaître, G., Keddaouche, K., 2013. The granite tors of Dartmoor, Southwest England: rapid and recent emergence revealed by Late Pleistocene cosmogenic apparent exposure ages. *Quat. Sci. Rev.* 61, 62–76.
- Hallet, B., Hunter, L., Bogen, J., 1996. Rates of erosion and sediment evacuation by glaciers: a review of field data and their implications. *Glob. Planet. Chang.* 12, 213–235.
- Herman, F., Seward, D., Valla, P.G., Carter, A., Kohn, B., Willett, S.D., Ehlers, T.A., 2013. Worldwide acceleration of mountain erosion under a cooling climate. *Nature* 504, 146–152.
- Heyman, J., Stroeven, A.P., Harbor, J.M., Caffee, M.W., 2011. Too young or too old: evaluating cosmogenic exposure dating based on an analysis of compiled boulder exposure ages. *Earth Planet. Sci. Lett.* 302, 71–80.
- Hicks, D.M., McSaveney, M.J., Chinn, T.J.H., 1990. Sedimentation in proglacial Ivory Lake, Southern Alps, New Zealand. *Arct. Alp. Res.* 22, 26–42.
- Hoek, W.Z., 2009. The last glacial-interglacial transition. *Episodes* 31, 226–229.
- Ivy-Ochs, S., Kerschner, H., Maisch, M., Christl, M., Kubik, P.W., Schlüchter, C., 2009. Latest Pleistocene and Holocene glacier variations in the European Alps. *Quat. Sci. Rev.* 28, 2137–2149.
- Koppes, M., Hallet, B., 2006. Erosion rates during rapid deglaciation in Icy Bay, Alaska. *J. Geophys. Res.* 111, F02023. <http://dx.doi.org/10.1029/2005JF000349>.
- Koppes, M.N., Montgomery, D.R., 2009. The relative efficacy of fluvial and glacial erosion over modern to orogenic timescales. *Nat. Geosci.* 2, 644–647.
- Koppes, M., Hallet, B., Rignot, E., Mouginit, J., Wellner, J.S., Boldt, K., 2015. Observed latitudinal variations in erosion as a function of glacier dynamics. *Nature* 526, 100–103.
- Korschinek, G., Bergmaier, A., Faestermann, T., Gerstmann, U.C., Knie, K., Rugel, G., Wallner, A., Dillmann, I., Dollinger, G., von Gostomski, C.L., Kossert, K., Maiti, M., Poutivsev, M., Remmert, A., 2010. A new value for the half-life of  $^{10}\text{Be}$  by heavy-ion elastic recoil detection and liquid scintillation counting. *Nuclear Instrumentation Methods in Physics Research, Section B: Beam Interactions with Materials and Atoms*. 268, pp. 187–191.
- Lal, D., 1991. Cosmic ray labeling of erosion surfaces: in situ nuclide production rates and erosion models. *Earth Planet. Sci. Lett.* 104, 424–439.
- Larsen, E., Mangerud, J., 1981. Erosion rate of a younger Dryas cirque glacier at Krakenes, western Norway. *Ann. Glaciol.* 2, 153–158.
- Li, Y., Harbor, J., Stroeven, A.P., Fabel, D., Kleman, J., Fink, D., Caffee, M., 2005. Ice sheet erosion patterns in valley systems in northern Sweden investigated using cosmogenic nuclides. *Earth Surf. Process. Landf.* 30, 1039–1049.
- Li, Y., Fabel, D., Stroeven, A.P., Harbor, J., 2008. Unraveling complex exposure-burial histories of bedrock surfaces under ice sheets by integrating cosmogenic nuclide concentrations with climate proxy records. *Geomorphology* 99, 139–149.
- Luetscher, M., Hoffmann, D.L., Frisia, S., Spötl, C., 2011. Holocene glacier history from alpine speleothems, Milchbach cave, Switzerland. *Earth Planet. Sci. Lett.* 302, 95–106.
- MacGregor, K.R., Anderson, R.S., Anderson, S.P., Waddington, E.D., 2000. Numerical simulations of glacial-valley longitudinal profile evolution. *Geology* 28, 1031–1034.
- Marquette, G.C., Gray, J.T., Gosse, J.C., Courchesne, F., Stockli, L., Macpherson, G., Finkel, R., 2004. Felsenmeer persistence under non-erosive ice in the Torngat and Kaumajet mountains, Quebec and Labrador, as determined by soil weathering and cosmogenic nuclide exposure dating. *Can. J. Earth Sci.* 41, 19–38.
- Martínez de Pisón, E., 1989. Morfología glacial del valle de Benasque (Pirineo Aragonés). *Eriu* 18, 51–64.
- Matthews, J.A., 2013. Neoglaciation in Europe. In: Elias, S.A., Mock, C.J. (Eds.), *Encyclopedia of Quaternary Science*, 2nd edn. 2. Elsevier, pp. 257–268.
- Merchel, S., Bremser, W., 2004. First international  $^{26}\text{Al}$  interlaboratory comparison – Part I. Nuclear Instrumentation Methods in Physics Research, Section B: Beam Interactions with Materials and Atoms. 223–224, pp. 393–400.
- Merchel, S., Hoppers, U., 1999. An update on radiochemical separation techniques for the determination of long-lived radionuclides via accelerator mass spectrometry. *Radiochim. Acta* 84, 215–219.
- Merchel, S., Arnold, M., Aumaître, G., Benedetti, L., Bourlès, D.L., Braucher, R., Alfimov, V., Freeman, S.P.H.T., Steier, P., Wallner, A., 2008. Towards more precise  $^{10}\text{Be}$  and  $^{36}\text{Cl}$  data from measurements at the 10 – 14 level: influence of sample preparation. Nuclear Instrumentation Methods in Physics Research, Section B: Beam Interactions with Materials and Atoms. 266, pp. 4921–4926.
- Metcalfe, J.R., Fitzgerald, P.G., Baldwin, S.L., Muñoz, J.A., 2009. Thermochronology of a convergent orogen: constraints on the timing of thrust faulting and subsequent exhumation of the Maladeta Pluton in the Central Pyrenean Axial Zone. *Earth Planet. Sci. Lett.* 287, 488–503.
- Millet, L., Rius, D., Galop, D., Heiri, O., Brooks, S.J., 2012. Chironomid-based reconstruction of Lateglacial summer temperatures from the Ech palaeolake record (French western Pyrenees). *Palaeogeogr. Palaeoclimatol. Palaeoecol.* 315–316, 86–99.
- Mills, H.H., 1979. Some implications of sediment studies for glacial erosion on Mount Rainier, Washington. *Northwest Sci.* 53, 190–199.
- Mîndrescu, M., Evans, I.S., 2014. Cirque form and development in Romania: allometry and the buzzsaw hypothesis. *Geomorphology* 208, 117–136.
- Mitchell, S.G., Humphries, E.E., 2014. Glacial cirques and the relationship between equilibrium line altitudes and mountain range height. *Geology* 43, 35–38.

- Mitchell, S.G., Humphries, E.E., 2015. Glacial cirques and the relationship between equilibrium line altitudes and range height. *Geology*:e367–e369 <http://dx.doi.org/10.1130/G37001Y.1>.
- Mitchell, S.G., Montgomery, D.R., 2006. Influence of a glacial buzzsaw on the height and morphology of the Cascade Range in central Washington State, USA. *Quat. Res.* 65, 96–107.
- Molnar, P., England, P., 1990. Late Cenozoic uplift of mountain ranges and global climate change: chicken or egg? *Nature* 346, 29–34.
- Nishiizumi, K., Imamura, M., Caffee, M.W., Southon, J.R., Finkel, R.C., McAninch, J., 2007. Absolute calibration of  $^{10}\text{Be}$  AMS standards. *Nuclear Instrumentation Methods in Physics Research, Section B: Beam Interactions with Materials and Atoms*. 258, pp. 403–413.
- Olyphant, G.A., 1981. Allometry and cirque evolution. *Geol. Soc. Am. Bull.* 92, 679–685.
- Ortuño, M., Queralt, P., Martí, A., Ledo, J., Masana, E., Perea, H., Santanach, P., 2008. The north Maladeta fault (Spanish central Pyrenees) as the Vielha 1923 earthquake seismic source: recent activity revealed by geomorphological and geophysical research. *Tectonophysics* 453, 246–262.
- Ortuño, M., Martí, A., Martín-Closas, C., Jiménez-Moreno, G., Martinetto, E., Santanach, P., 2013. Palaeoenvironments of the Late Miocene Prüedo Basin: implications for the uplift of the Central Pyrenees. *J. Geol. Soc. Lond.* 170, 79–92.
- Penck, A., 1919. Die Gipfflur der Alpen. *Sitzungsberichte der Preussischen Akademie der Wissenschaften, Berlin*. 17, pp. 256–268.
- Phillips, W.M., Hall, A.M., Mottram, R., Fifield, L.K., Sugden, D.E., 2006. Cosmogenic  $^{10}\text{Be}$  and  $^{26}\text{Al}$  exposure ages of tors and erratics, Cairngorm Mountains, Scotland: time-scales for the development of a classic landscape of selective linear glacial erosion. *Geomorphology* 73, 222–245.
- Putkonen, J., Swanson, T., 2003. Accuracy of cosmogenic ages for moraines. *Quat. Res.* 59, 255–261.
- Putkonen, J., Connolly, J., Orloff, T., 2008. Landscape evolution degrades the geologic signature of past glaciations. *Geomorphology* 97, 208–217.
- Rasmussen, S.O., Bigler, M., Blockley, S.P., Blunier, T., Buchardt, S.L., Clausen, H.B., Cvijanovic, I., Dahl-Jensen, D., Johnsen, S.J., Fischer, H., Gkinis, V., Guillemin, M., Hoek, W.Z., Lowe, J.J., Pedro, J.B., Popp, T., Seierstad, I.K., Steffensen, J.P., Svensson, A.M., Vallelonga, P., Vinther, B.M., Walker, M.J.C., Wheatley, J.J., Winstrup, M., 2014. A stratigraphic framework for abrupt climatic changes during the Last Glacial period based on three synchronized Greenland ice-core records: refining and extending the INTIMATE event stratigraphy. *Quat. Sci. Rev.* 106, 14–28.
- Reheis, M.J., 1975. Source, transportation and deposition of debris on Arapaho glacier, Front Range, Colorado, USA. *J. Glaciol.* 14, 407–420.
- Reille, M., Andrieu, V., 1993. Variations de la limite supérieure des forêts dans les Pyrénées (France) pendant le Tardiglaciaire. *Comptes-Rendus de l'Académie des Sciences, Série D*. 272, pp. 3112–3115.
- René, P., 2008. Les glaciers actuels des Pyrénées. In: Canérot, J., Colin, J.-P., Platel, J.-P., Bilotte, M. (Eds.), *Pyrénées d'hier et d'aujourd'hui*. Atlantica, Biarritz, pp. 163–176.
- René, P., 2011. Régression des glaciers pyrénéens et transformation du paysage depuis le Petit Âge glaciaire. *Sud-Ouest Européen*. 32 pp. 5–19.
- René, P., 2013. Glaciers des Pyrénées, le réchauffement climatique en images. *Cairn édition* (166 p).
- Rigo, A., Vernant, P., Feigl, K.L., Goula, X., Khazaradze, G., Talaya, J., Morel, L., Nicolas, J., Baize, S., Chery, J., Sylvander, M., 2015. Present-day deformation of the Pyrenees revealed by GPS surveying and earthquake focal mechanisms until 2011. *Geophys. J. Int.* 201, 947–964.
- Robl, J., Prasicek, G., Hergarten, S., Salcher, B., 2015a. Glacial cirques and the relationship between equilibrium line altitudes and range height. *Geology*, e365 <http://dx.doi.org/10.1130/G36757C.1>.
- Robl, J., Prasicek, G., Hergarten, S., Stüwe, K., 2015b. Alpine topography in the light of tectonic uplift and glaciation. *Glob. Planet. Chang.* 127, 34–49.
- Samworth, E.A., Warburton, E.K., Engelbertink, G.A.P., 1972. Beta decay of the  $^{26}\text{Al}$  ground state. *Phys. Rev. C* 5, 138–142.
- Sanders, J.W., Cuffey, K.M., MacGregor, K.R., Collins, B.D., 2013. The sediment budget of an alpine cirque. *Geol. Soc. Am. Bull.* 125, 229–248.
- Scherler, D., 2015. Climatic limits to headwall retreat in the Khumbu Himalaya, eastern Nepal. *Geology* 42, 1019–1022.
- Schmidt, K.M., Montgomery, D.R., 1995. Limits to relief. *Science* 270, 617–620.
- Shuster, D.L., Ehlers, T.A., Rusmoren, M.E., Farley, K.A., 2005. Rapid glacial erosion at 1.8 Ma revealed by  $^4\text{He}/^3\text{He}$  thermochronometry. *Science* 310, 1668–1670.
- Shuster, D.L., Cuffey, K.M., Sanders, J.W., Balco, G., 2011. Thermochronometry reveals headward propagation of erosion in an alpine landscape. *Science* 332, 84–88.
- Simonneau, A., Doyen, E., Chapron, E., Millet, L., Vannièr, B., Di Giovanni, C., Bossard, N., Tachikawa, K., Bard, E., Albéric, P., Desmet, M., Roux, G., Lajeunesse, P., Berger, J.F., Arnaud, F., 2013. Holocene land-use evolution and associated soil erosion in the French Prealps inferred from Lake Paladru sediments and archaeological evidences. *J. Archaeol. Sci.* 40, 1636–1645.
- Small, E.E., Anderson, R.S., 1995. Geomorphically driven late Cenozoic rock uplift in the Sierra Nevada, California. *Science* 270, 277–280.
- Solomina, O.N., Bradley, R.S., Hodgson, D.A., Ivy-Ochs, S., Jomelli, V., Mackintosh, A.N., Nesje, A., Owen, L.A., Wanner, H., Wiles, G.C., Young, N.E., 2015. Holocene glacier fluctuations. *Quat. Sci. Rev.* 111, 9–34.
- Staiger, J.K.W., Gosse, C.G., Johnson, J.V., Fastook, J., Gray, J.T., Stockli, D.F., Stockli, L., Finkel, R., 2005. Quaternary relief generation by polythermal glacier ice. *Earth Surf. Process. Landf.* 30, 1145–1159.
- Sternai, P., Herman, F., Champagnac, J.-D., Fox, M., Salcher, B., Willett, S.D., 2015. Preglacial topography of the European Alps. *Geology* 40, 1067–1070.
- Stone, J.O., 2000. Air pressure and cosmogenic isotope production. *J. Geophys. Res.* 105, 23753–23759.
- Stroeven, A.P., Fabel, D., Harbor, J., Hättestrand, C., Kleman, J., 2002. Quantifying the erosional impact of the Fennoscandian ice sheet in the Torneträsk–Narvik corridor, northern Sweden, based on cosmogenic radionuclide data. *Geogr. Ann.* 84A, 275–287.
- Thomson, S.N., Brandon, M.T., Tomkin, J.H., Reiners, P.W., Vasquez, C., Wilson, N.J., 2010. Glaciation as a destructive and constructive control on mountain building. *Nature* 467, 313–317.
- Valla, P.G., Shuster, D.L., van der Beek, P.A., 2011. Significant increase in relief of the European Alps during mid-Pleistocene glaciations. *Nat. Geosci.* 4, 688–692.
- Van Kolschoten, T., Gibbard, P.L., Knudsen, K.-L., 2003. The Eemian interglacial, a global perspective: introduction. *Glob. Planet. Chang.* 36, 147–149.
- Vergés, J., Fernández, M., Martínez, A., 2002. The Pyrenean orogen: pre-, syn-, and post-collisional evolution. In: Rosenbaum, G., Lister, G. (Eds.), *Reconstruction of the Evolution of the Alpine-Himalayan Orogen*. *Journal of the Virtual Explorer* 8. <http://dx.doi.org/10.3809/jvirtex.2002.00058>.
- Whipple, K.X., 2009. The influence of climate on the tectonic evolution of mountain belts. *Nat. Geosci.* 2, 97–104.
- Whipple, K.X., Kirby, E., Brocklehurst, S.H., 1999. Geomorphic limits to climate-induced increases in topographic relief. *Nature* 401, 39–43.
- Wohlfarth, B., 1996. The chronology of the last termination: a review of radiocarbon-dated, high-resolution terrestrial stratigraphies. *Quat. Sci. Rev.* 15, 267–284.